

Tuning the optoelectronic properties of graphene quantum dots by BN-ring doping: A density functional theory study

Samayita Das^{1,*} and Alok Shukla^{1,†}

¹*Department of Physics, Indian Institute of
Technology Bombay, Powai, Mumbai 400076, India*

arXiv:2603.15906v1 [cond-mat.mtrl-sci] 16 Mar 2026

Abstract

Graphene monolayer is a material with zero band gap, because of which its applications in optoelectronics are limited. The question arises, can we modify the optoelectronic properties of graphene by doping it with other atoms? Synthesis of 2D monolayer of graphene doped with heteroatoms such as boron and nitrogen, and a few computational studies of their structural and electronic properties were previously reported. In this work, we aim to answer this question for graphene quantum dots (GQDs), i.e., how can we tune their optoelectronic performance by replacing their carbon rings with $(\text{BN})_3$ (borazine) hexagonal rings? In this work, we have studied in detail the geometry, electronic structure, and optical absorption spectra of fourteen different borazine-ring doped diamond-shaped GQDs, using a computational methodology based on the first-principles density functional theory (DFT). We refer to the doped structures as BN-GQDs, which differ from each other in the location, orientation and the number of borazine rings. We computed their optical absorption spectra using the time-dependent density-functional theory (TDDFT), and carefully examined: (a) for the single-ring doped BN-GQDs the influence of the location of the ring on their optical properties, and (b) for the double ring doped systems, the influence of the location, mutual distance and orientation of the rings on their absorption spectra. Frontier molecular orbitals of all the structures considered here are studied in detail in order to understand the nature of low-lying optical excitations. We also analyzed the point-group symmetries of considered BN-GQDs, and performed a group-theoretic analysis of the influence of their reduced symmetries, on their optical properties. Our results indicate that BN-ring doping can achieve a significant control over the optical properties of GQDs. The comparison of the optical absorption spectra of the BN-GQDs with the parent GQD shows remarkable spectral broadening with optical gap spanning over infrared to visible region of the spectrum. Thus, systematic BN-ring doping provides easy tunability of the electronic and optical properties of BN-GQDs to a considerable extent which is very promising for their optoelectronic applications.

* samayitadas5@gmail.com

† shukla@iitb.ac.in

I. INTRODUCTION

Graphene quantum dots with hetero-atom doping have emerged as a new class of π -conjugated molecules that are highly useful in the field of optoelectronics [1–3]. Because of their high degree of tunability, structural flexibility, low costs of synthesis and miniaturization, they can easily replace the conventional Si-based technology that has several drawbacks. In particular, the silicon based devices exhibit structural stiffness, moderate tunability, low carrier mobility, and high production costs. It is widely believed that these problems can be easily solved by shifting to graphene-based materials that have high carrier mobility [4], thermal and chemical stability [5] and most importantly electronic and optical tunability that can be controlled by doping [6, 7]. Although graphene has many exceptional properties, its zero band gap [4] makes it unsuitable for many optoelectronic applications. Quantum confinement is one of the ways to overcome this problem by working with reduced dimensional nanostructures such as 1D graphene nanoribbons (GNRs) [8, 9] and 0D graphene quantum dots (GQDs) [10–12]. GQDs exhibit higher band gap as compared to GNRs depending on their size and shape [13], which makes GQDs popular for applications such as organic light emitting diodes [14–16], solar cells [17, 18], and organic field-effect transistors (OFETs) [19–21]. Quantum confinement is surely an efficient way of introducing band gap in graphene, but controllable tuning of its electronic and optical properties is very important for advanced optoelectronic applications. Another effective way of controlling the band gap is through hetero-atom doping, which normally reduces the symmetry of the system. For graphene, various doping techniques have been explored in the past [22–24]; however, a natural way to dope it is by substituting sp^2 hybridized carbon atom pairs by isoelectronic BN units that also participate in the planar sp^2 bonding, giving rise to stable π -conjugated structures just like the parent material but with distinct electronic and optical properties.

In the past, Xu *et al.* [25] performed large-scale systematic first-principles density-functional theory (DFT) calculations on graphene superlattices doped by BN units and studied the evolution of their electronic and magnetic properties. They reported that the band gap of the superlattice increases with the size of the BN nanodots regardless of the shape of the dopants. On the other hand, Ajeel *et al.* [26] considered a coronene molecule ($C_{24}H_{12}$) and co-doped it by single B and N atoms (paired or separated) at various places,

and studied the evolution of its electronic and vibrational properties using the first-principles DFT approach. They found that the HOMO-LUMO gap decreases upon doping as compared to the pristine GQD. As far as experimental works are concerned, BN-doped GQDs (BN-GQDs) were synthesized by Fei *et al.* [27] and were used as catalysts for the oxygen reduction reaction. The authors concluded that BN doping leads to a far superior catalytic performance. Li *et al.* [28] synthesized and studied the optical properties of BN-GQDs with the aim of their applications in bio-imaging. They found that the BN-doped GQDs emitted in the yellow with a high quantum yield. Yang *et al.* [29] also synthesized BN-GQDs, and studied their optical properties for their possible applications as fluorescence sensors for the detection of Hg^{2+} and F^- ions. They also reported high fluorescence quantum yields and life times for the BN-doped GQDs. Budak *et al.* [30] synthesized BN-GQDs using a bottom-up synthesis approach, and reported boron-regulated dual emission in their nanostructures with possible applications in white light-emitting diodes (LEDs) and solar cells. From a synthesis point of view, the field of BN-doped π -conjugated molecules was comprehensively reviewed recently by Chen *et al.* [31].

However, the carbon-based structures discussed above were either doped with a bonded BN pair, or separated B and N atoms, not doped with $(\text{BN})_3$ -ring structures. The ring-based $(\text{BN})_3$ -doped graphene structures were successfully synthesized by Sánchez-Sánchez *et al.* [32], and Chen *et al.* [33], while Herrera-Reinoza *et al.* [34] synthesized nanographenes doped by h-BN clusters consisting of multiple $(\text{BN})_3$ rings, and reported the opening of a band gap in the range 1.4–1.6 eV for a doping concentration of about 17%. By means of a first-principles DFT approach, Caputo *et al.* [35] studied the influence of doping graphene with hexagonal $(\text{BN})_3$ rings on its electronic and structural properties. They found that for all the considered cases, the structure remained planar, and demonstrated significant variation in the band gap with the changing doping concentration and pattern. Inspired by their work, we decided to explore the influence of doping finite graphene fragments, i.e., GQDs by the $(\text{BN})_3$ rings with the aim of studying the evolution of their electronic and optical properties.

It is well known that doping a quantum dot introduces dopants as scattering sites for the charge carriers. As the charge carriers move through the material, the scattering events reduce their mean free path and consequently, the mobility. The change in mobility, which has a significant impact on the transport properties, can be controlled by different doping

strategies [36–38]. However, in this work we have mainly focused on tuning the optoelectronic properties of the BN-GQDs in terms of systematic BN-ring doping. For the purpose, we have employed a first-principles DFT-based methodology in which the optical absorption spectra have been computed using the TDDFT approach. We have chosen a diamond-shaped GQD ($C_{30}H_{14}$) of D_{2h} symmetry as the host for the doping, and have demonstrated a high degree of tunability in its electro-optical properties depending on the number, location and orientation of the $(BN)_3$ rings.

The remainder of the paper is organized as follows. In Sec. II, we briefly describe our computational methodology, followed by a detailed presentation and discussion of our results in Sec. III. Finally, we present our conclusions in Sec. IV.

II. COMPUTATIONAL DETAILS

We start our study with the geometry optimization of the considered structures, for which we employed a first-principles all-electron density functional theory (DFT) approach, along with the atom-centered Cartesian Gaussian basis functions, as implemented in the Gaussian16 package [39]. Because of the all-electron nature of the calculations, no pseudopotentials were employed in these calculations. As far as the exchange-correlation functional is concerned, unless otherwise specified, we used the B3LYP [40–42] hybrid functional both for the ground-state properties as well as for the calculations of the optical absorption spectra employing the time-dependent density functional theory (TDDFT) [43, 44] approach. These calculations were performed using valence double zeta basis set 6-31++G(d,p) which includes both the polarization and diffuse functions [45, 46]. The presence of polarization function in basis set, ensures flexibility of chemical bond formation, while the small-exponent diffuse functions help in accurately predicting quantities such as the dipole moments. The convergence criteria of 10^{-8} Hartree was set to solve the Kohn-Sham equations [47] self consistently, while for the geometry optimization, the threshold values of gradient forces between each constituent atoms, average (RMS) force, maximum displacement and average (RMS) displacement were set at 0.000450 Hartree/Bohr, 0.00030 Hartree/Bohr, 0.00180 Bohr, and 0.00120 Bohr, respectively. The stability of the computed structures was confirmed by performing vibrational frequency analysis. Based on these optimized structures, the optical absorption spectra of various BN-GQDs were calculated using the TDDFT approach, incor-

porating the same exchange-correlation functional and the basis set in Gaussian16 software which employs an adiabatic frequency-space-based implementation [48–54]. Recently using the same functional and basis set we obtained excellent agreement on optical absorption of some GQDs with the experimental results [55]. However, here for comparison purpose we have calculated the optical absorption spectra using HSE06 functional also and the results obtained are in excellent agreement with the corresponding B3LYP ones, as shown in the Fig. S2 within the Supplemental Material (SM) [56]. Here we have also presented results of total density of states (TDOS) and partial density of states (PDOS) of the BN-GQDs, and for that purpose we have used Multiwfn software [57].

III. RESULTS AND DISCUSSION

A. Optimized structures and stability

The dangling bonds of the edge atoms in all the structures considered in this work were saturated with the hydrogen atoms. First we have optimized the geometry of the diamond-shaped pristine GQD containing thirty carbon atoms ($C_{30}H_{14}$), and its optimized structure is presented in Fig. 1. This GQD contains nine aromatic hexagonal rings, and it is a polycyclic aromatic hydrocarbon named dibenzo[bc,kl]coronene of the D_{2h} symmetry. Next, we dope the pristine GQD by replacing the hexagonal carbon rings (C_6) with the corresponding $(BN)_3$ rings, obtaining 14 distinct structures with different symmetries. In all the cases, the optimized geometries were found to be planar 2D structures, i.e., no buckling was observed. Subsequently, we performed the vibrational-frequency analysis on all the optimized structures (pristine as well as doped), and no imaginary frequencies were found indicating that the considered structures are dynamically stable. For the pristine structure (dibenzo[bc,kl]coronene), the minimum and maximum C–C bond lengths are 1.358 Å (C29–C30) and 1.445 Å (C13–C14) respectively, the parentheses following the bond lengths indicate the carbon atoms involved in the bonds, according to the atom numbering scheme displayed in Fig. 1. The edge C–H bond lengths ranged from 1.086 to 1.088 Å, while for the BN-GQDs in which the edge C atoms were substituted by B/N atoms, the B–H bond lengths were close to 1.19 Å, and the N–H bond lengths were nearly 1.01 Å in all the cases. For BN-GQDs, the optimized geometries have the values of C–C, C–H bond lengths very close

to the optimized pristine structure, and other bond lengths (B–N, B–C, N–C) present in the doped structures have average value close to the ideal value 1.4 Å. All the optimized bond lengths indicating their minima and maxima are presented in Table S1 within the SM [56].

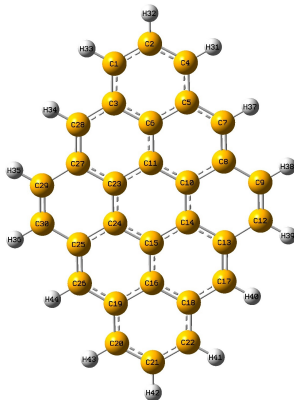


Figure 1. Optimized geometry of pristine diamond-shaped GQD (dibenzo[bc,kl]coronene, $C_{30}H_{14}$).

As far as the pristine GQD is concerned, the optimized minimum and maximum bond angles are 118.0° (C12-C13-C14) and 122.0° (C13-C17-C18), respectively. The average bond lengths and angles in the pristine and doped structures are close to the standard values of 1.4 Å and 120° , respectively. For the doped structures, all the optimized angles indicating their minima and maxima are shown in Table S2 within the SM [56].

We have categorized the doped structures into three types based on the number, location, and mutual orientation of the dopants (borazine rings). The first category corresponds to doping with a single $(BN)_3$ ring, for which four unique structures are possible depending on the locations of the dopants as shown in Fig. 2(a). The next category corresponds to doping with two fused $(BN)_3$ rings, for which also four possibilities are there depending on their locations as shown in Fig. 2(b). Finally, we have substituted two separated benzene rings with two $(BN)_3$ rings in the pristine GQD, which resulted in three possible structures; furthermore, for each of these three structures there are two possibilities depending on the mutual orientation of the two rings. The structures in which the two rings have parallel orientation are denoted by two up arrows $\uparrow\uparrow$, while those with opposite orientation are indicated by up and down arrows $\uparrow\downarrow$. Based on this characterization scheme, six model

structures are possible as depicted in Fig. 2(c). Thus, in this work, we have considered a total of 14 different $(\text{BN})_3$ -ring doped diamond shaped graphene quantum dots.

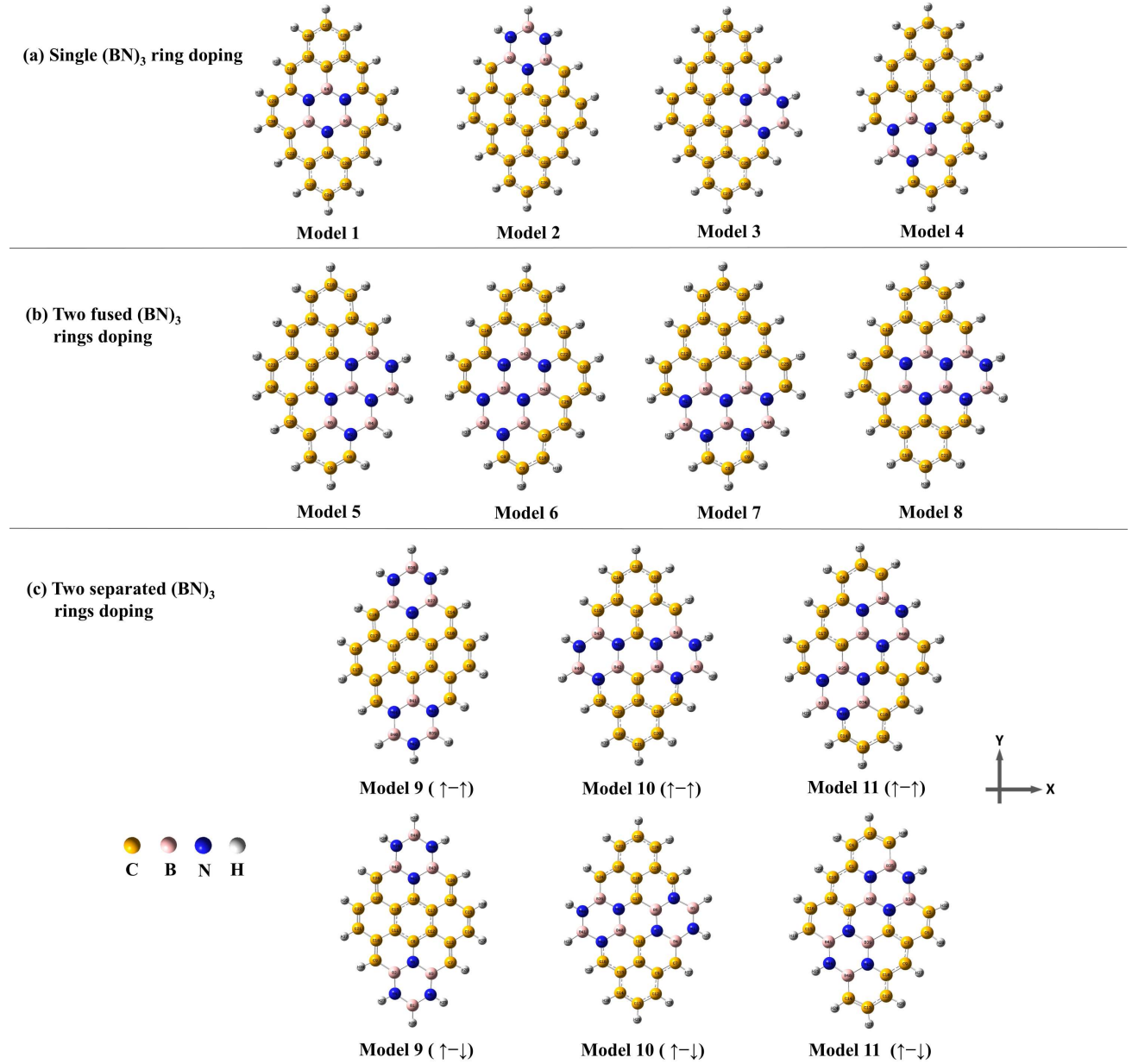


Figure 2. Diamond-shaped BN-GQDs with different doping schemes. In the last category of two separated $(\text{BN})_3$ rings doped structures (models 9-11), up-up and up-down arrows inside the parentheses represent the parallel and antiparallel orientations of the two BN rings with respect to each other.

Because of the hetero-atomic nature of the dopant rings, we wanted to quantify the induced ionicity in the doped structures. Therefore, we performed Mulliken charge analysis on all the BN-GQDs and found that the N atoms acquire negative charges, while B atoms acquire positive charges. The C atoms, on the other hand, exhibit both positive and negative charges based on their proximity to B/N atoms. This behavior can be understood quantitatively in terms of the electronegativities of the atoms involved. Since the B atoms have the least electronegativity (2.04) as compared to the N and C atoms, they will lose electrons easily and acquire positive charges, while the N atoms have the highest electronegativity (3.04) among the three, they easily attract electrons and become negatively charged. But, the electronegativity of C atoms (2.55) is in between of B and N atoms, so they exhibit both positive and negative charges based on which atom they are bonded with. Electronegativity of H atoms (2.20) is higher than B atoms but lower compared to the C and N atoms, therefore, the H atoms connected to C and N atoms acquire positive charges, while those connected with the B atoms have negative charges. However, given the electrical neutrality of the considered systems, the sum of all the induced Mulliken charges on every BN-GQD is zero.

B. Cohesive energies

Energetic stability of all the structures considered in this work can be analyzed based on the cohesive energy (or binding energy) per atom calculated using the formula, $E_{coh} = \frac{1}{N_{total}} (E_{total} - n_C E_C - n_H E_H - n_B E_B - n_N E_N)$, where N_{total} , n_C , n_H , n_B , n_N are, respectively, the total number of atoms, and the numbers of C, H, B, and N atoms present in the BN-GQD structures. The calculated optimized energies of the BN-GQDs are denoted by E_{total} , while E_C , E_H , E_B , E_N are, respectively, the calculated total energies of the isolated C, H, B, N atoms. The computed cohesive energies are presented in Table I from which the following trends are obvious: (a) all the cohesive energies are negative implying that all the structures are energetically stable; (b) the BN-GQDs with the lowest magnitudes of cohesive energies (≈ 4.4 eV) correspond to models 5, 6, 7, and 8, each of which is doped by two fused (BN)₃ rings; (c) the rest of the structures, whether doped with a single (BN)₃ ring or with two separated rings, have significantly larger cohesive energies in excess of 6.5 eV/atom; and (d) comparatively speaking, the structures doped by single ring have cohesive

energies ≈ 0.2 eV higher than the ones doped by two separated rings.

Quantum dots	Cohesive energy/atom (eV)
Pristine	-6.945
Model 1	-6.730
Model 2	-6.752
Model 3	-6.726
Model 4	-6.724
Model 5	-4.398
Model 6	-4.398
Model 7	-4.374
Model 8	-4.383
Model 9 ($\uparrow - \uparrow$)	-6.548
Model 9 ($\uparrow - \downarrow$)	-6.558
Model 10 ($\uparrow - \uparrow$)	-6.504
Model 10 ($\uparrow - \downarrow$)	-6.512
Model 11 ($\uparrow - \uparrow$)	-6.514
Model 11 ($\uparrow - \downarrow$)	-6.528

Table I. Cohesive energy per atom for all the structures considered in this work.

C. Electronic structure

1. Frontier molecular orbitals

In order to understand the optical and electronic properties of the BN-GQDs considered here, we need to understand the nature of their frontier molecular orbitals (MOs), i.e., HOMO (highest occupied molecular orbital) and LUMO (lowest unoccupied molecular orbital), and their energies. The plots of these orbitals for the pristine GQD are presented in Fig. 3 while those for various doped structures are shown in Fig. 4. It is obvious from the figures that HOMO/LUMO orbital for both the pristine and doped structures are of

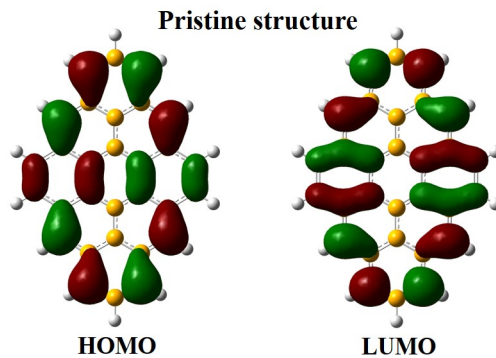


Figure 3. Plots of HOMO (H) and LUMO (L) orbitals of pristine diamond shaped graphene quantum dot.

π/π^* type, delocalized over C, B, and N atoms, but with negligible charge densities on the passivating H atoms. Although, we have not plotted the MOs further away from the Fermi level, there are several π/π^* type orbitals in the lower energy range in spite of doping. This implies that in addition to C atoms, both B and N atoms also contribute to the π conjugation in a way similar to polycyclic aromatic hydrocarbons (PAHs) which the parent pristine molecule is. As a result, we expect the low-lying optical excitations of these materials to be dominated by $\pi \rightarrow \pi^*$ transitions.

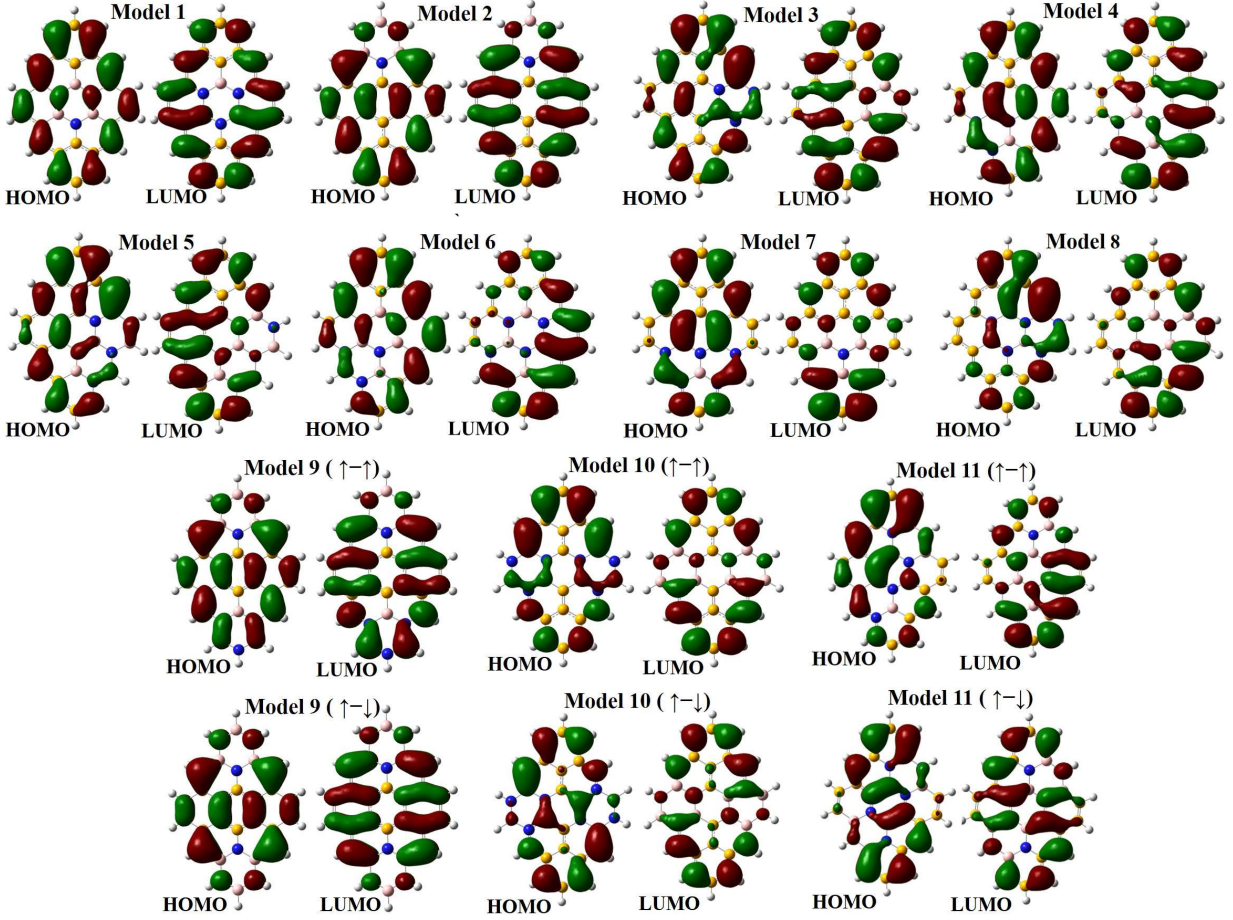


Figure 4. Plots of HOMO (H) and LUMO (L) orbitals of different BN-GQDs. The doping model is written on top of each figure.

2. Density of states

In Fig. 5 we present both the total density of states (TDOS) along with the atom projected density of states (PDOS) for the pristine GQD as well as a few doped BN-GQDs. We note the following trends: (a) as expected, DOS is negligible in the region between the HOMO-LUMO energies; (b) on the occupied side of the energy, the maximum contribution is from carbon atoms; and (c) in the unoccupied region of the orbital energies, in addition to carbon, other atoms also contribute significantly away from the LUMO. However, for all the systems considered, near the HOMO/LUMO orbital energies, the dominant contributions to the DOS are from the carbon atoms. Corresponding orbital projected DOS plots are presented in Fig. S1 within the SM [56]. From the DOS plots it is again confirmed that the MOs near Fermi level are of π and π^* type.

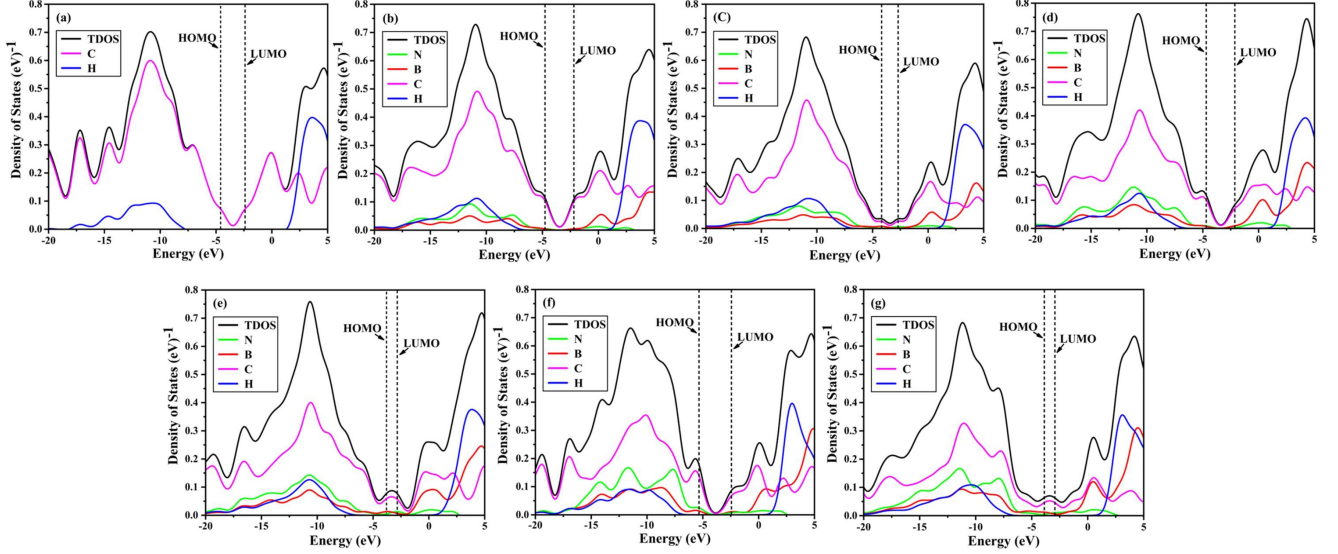


Figure 5. Total and atom projected DOS plots for: (a) pristine GQD, (b) single BN-ring doping (model 1), (c) single BN-ring doping (model 3), (d) fused double BN-ring doping (model 6), (e) fused double BN-ring doping (model 7), (f) separated double BN-ring doping [model 9 ($\uparrow - \downarrow$)], and (g) separated double BN-ring doping [model 10 ($\uparrow - \uparrow$)].

3. HOMO-LUMO Gaps

In Table II, we list the values of the orbital energies of the H/L orbitals, along with the corresponding H-L gaps.

From the table it is obvious that models 1, 2, 6 and 9 have larger H-L gaps as compared to the pristine structure, while the rest of the structures have lower values. This is quite a remarkable result considering the fact that h-BN monolayer is a wide band gap insulator while graphene is gapless. Therefore, one would think that doping of GQDs with BN rings will widen the gap, however, as our results suggest, it is happening in a small number of geometries, while for most of the structures, the gap actually reduces on doping. To further understand this, we examine the behavior of HOMO/LUMO orbital energies on doping. We note that for the models 1, 2, 6 and 9, as compared to the pristine case, the HOMO energies become lower, while the LUMO energies, except for model 2 and model 9 ($\uparrow - \downarrow$), move a bit higher.

Table II. The calculated B3LYP values of the orbital energies corresponding to HOMO (E_{HOMO}), LUMO (E_{LUMO}), and the H-L gaps (E_{HL}) for the pristine and BN-GQDs.

Quantum dots	E_{HOMO} (eV)	E_{LUMO} (eV)	E_{HL} (eV)
Pristine	-4.86	-2.68	2.18
Model 1	-5.04	-2.48	2.56
Model 2	-5.23	-2.73	2.50
Model 3	-4.46	-2.99	1.47
Model 4	-4.66	-2.71	1.96
Model 5	-4.48	-2.88	1.61
Model 6	-4.97	-2.43	2.54
Model 7	-4.08	-3.13	0.95
Model 8	-4.25	-3.13	1.12
Model 9 ($\uparrow - \uparrow$)	-5.08	-2.23	2.86
Model 9 ($\uparrow - \downarrow$)	-5.64	-2.76	2.88
Model 10 ($\uparrow - \uparrow$)	-4.17	-3.23	0.94
Model 10 ($\uparrow - \downarrow$)	-4.25	-3.12	1.13
Model 11 ($\uparrow - \uparrow$)	-4.46	-2.95	1.51
Model 11 ($\uparrow - \downarrow$)	-4.56	-3.10	1.45

For the remaining models, we note that the LUMO energies move significantly lower as compared to the pristine case, while the HOMO energies move up, leading to the reduced H/L gaps. Recently, Caputo *et al.* [35], using a first-principles DFT-based approach, studied the influence of doping graphene monolayer with single and double B_3N_3 rings on its electronic properties. For the purpose, they considered diamond-shaped supercells similar to our pristine GQD, but of varying sizes, and reported that in all considered cases, a finite band gap opens. They reported GGA-PBE level band gaps of single BN ring doped structures in the range 0.31-1.54 eV, for different doping concentrations; while our results of B3LYP H-L gaps for the single BN ring doped GQDs (models 1-4) are in the range 1.47-2.56 eV. Clearly, the higher H-L gaps for BN-GQDs are from quantum confinement effects because of

their finite sizes. The noteworthy point is that when graphene is doped with BN rings, the gap always increases compared to the parent system. However, as discussed above, when the parent material is a GQD, the H-L gap increases in a few cases, while it decreases in a majority of the cases.

4. *Optical gaps*

Optical gap is defined as the lowest energy transition from ground state to the first dipole allowed excited state corresponding to the first peak in the optical absorption spectra. We have performed electron-correlated calculations of the optical gaps and the absorption spectra of all the QDs considered in this work using the TDDFT approach, with the B3LYP and HSE06 functionals, as implemented in the Gaussian16 program [39]. In the TDDFT method, the many-electron wave function of a system is considered to be a linear combination of the Kohn-Sham (KS) ground state, along with all possible electron-hole (e-h) type singly-excited configurations obtained from the KS state, thereby including the excitonic effects. This inclusion of the excitonic effects leads to a change in the energy gaps as compared to the KS calculations, which is evident in our calculations as well, in which a majority of optical gaps listed in Table III are larger than the corresponding H-L gaps listed in Table II. However, for models 1, 6, 9 ($\uparrow - \uparrow$), and 9 ($\uparrow - \downarrow$), we note slight reductions in the optical gaps as compared to the H-L gaps.

From the TDDFT values of the optical gaps presented in Table III, we see that there are insignificant quantitative differences in the gaps computed using two functionals. Furthermore, we note that in comparison to the pristine GQD, the optical gaps of the doped structures follow the same trends as the H-L gaps, i.e., for models 1, 2, 6, and 9, the optical gaps are larger than that of the pristine structure, while for the rest of the structures they are smaller. This is because the TDDFT wave functions of the excited states of the BN-GQDs corresponding to their optical gaps are dominated by HOMO-LUMO single-particle transition. Therefore, we conclude that even after accounting for the electron correlations, the qualitative behavior of optical gaps remains the same as of H-L gaps with respect to the doping configurations.

As far as the accuracy of our TDDFT calculations is concerned, we note that for the pristine GQD (dibenzo[bc,kl]coronene, $C_{30}H_{14}$) experimental value of its optical gap was

reported by Clar *et al.* [58] to be 2.55 eV, which is ≈ 0.2 eV higher than our calculated values. Therefore, we expect similar agreement for our calculated values of the optical gaps of BN-GQDs with the experiments, as and when they are performed.

Table III. The values of the optical gaps of pristine and BN-ring doped quantum dots calculated using the TDDFT approach, employing B3LYP and HSE06 functionals. The point-group symmetries of various BN-GQDs are also indicated.

Types of QDs	Doping configurations	Symmetry	TDDFT values of optical gaps (eV)	
			B3LYP	HSE06
Pristine	—	D_{2h}	2.31	2.34
Doped with single (BN) ₃ ring	Model 1	C_{2v}	2.52	2.54
	Model 2	C_{2v}	2.53	2.57
	Model 3	C_s	1.71	1.74
	Model 4	C_s	2.09	2.13
Doped with two fused (BN) ₃ rings	Model 5	C_s	1.77	1.79
	Model 6	C_s	2.44	2.45
	Model 7	C_{2v}	1.17	1.19
	Model 8	C_s	1.23	1.24
Doped with two separated (BN) ₃ rings	Model 9 ($\uparrow - \uparrow$)	C_{2v}	2.75	2.78
	Model 9 ($\uparrow - \downarrow$)	D_{2h}	2.79	2.79
	Model 10 ($\uparrow - \uparrow$)	C_{2v}	1.27	1.29
	Model 10 ($\uparrow - \downarrow$)	C_{2h}	1.46	1.49
	Model 11 ($\uparrow - \uparrow$)	C_s	1.59	1.61
	Model 11 ($\uparrow - \downarrow$)	C_{2h}	1.73	1.75

From Table III, we can see that the changes in the optical gaps, as compared to the pristine GQD, are sensitive to the doping pattern. Next, we aim to arrive at a broad understanding of this in terms of orbital localization (or delocalization) as compared to the pristine GQD. From the spatial distribution of frontier molecular orbitals (see Fig. 3) we can see that for the case of the pristine GQD, HOMO and LUMO orbitals are delocalized with electron density evenly spreading over the carbon framework. But doping with BN ring (because of the differing electronegativities of B and N, compared to C) disrupts the uniform

electron distribution of the pristine GQD, causing changes in the charge distributions of the frontier orbitals (see Fig. 4), leading to significant changes in the H-L energy gaps, and consequently in the optical gaps. Model 7 with fused double BN-rings exhibits the lowest value of the optical gap. Its HOMO/LUMO orbital plots reveal that the doping significantly delocalizes the HOMO charge distribution, thus raising its energy, while the LUMO is highly localized around a few atoms resulting in a lower energy. Thus, the H-L and optical gaps in this model get significantly redshifted as compared to the pristine GQD. On the other hand, model 9 doped with two separated and oppositely oriented BN-rings [model 9 ($\uparrow - \downarrow$)], has the highest value of the optical gap. In this unique configuration, doping stabilizes the HOMO by lowering its energy and, as compared to the pristine GQD, localizing its charge distribution. However, the charge distribution, and hence the energy of the LUMO, remains relatively unchanged, leading to a wider H-L gap and a blue-shift in the absorption spectrum. As far as other doped models are concerned, we can use similar arguments to explain the changes in their optical gaps as compared to the pristine GQD.

D. Optical absorption spectra

The optical gap contains information about the lowest optical excitation (H-L transition in this case), but the extended systems such as the ones considered here have similar excitations at higher energies as well, involving transitions among orbitals further away from the Fermi level. Therefore, the aim of this section is to study the absorption spectra of the pristine and doped structures beyond their optical gap, extending to higher energies. The spectra were computed using the well-known sum-over-states (SOS) formula,

$$\sigma(\omega) = 4\pi\alpha \sum_i \frac{\omega_{i0} |\langle i | \hat{e} \cdot \mathbf{r} | 0 \rangle|^2 \gamma^2}{(\omega_{i0} - \omega)^2 + \gamma^2}, \quad (1)$$

where $|0\rangle$ ($|i\rangle$) denotes the ground (excited) state TDDFT wave function, $\hbar\omega_{i0} = E_i - E_0$ is the energy difference between the two states, $\langle i | \hat{e} \cdot \mathbf{r} | 0 \rangle$ represents the corresponding transition dipole matrix element for an incident photon of energy $\hbar\omega$ polarized along the \hat{e} direction, α is the fine-structure constant, and γ is the uniform line width assumed for all excited states. For each QD, we considered 30 excited states in the SOS formula, and confirmed the convergence in a few cases by performing calculations with 40 excited states (see Fig. S3 within the SM [56]). Additionally, we also performed calculations of the absorption spectra

using the HSE06 functional for the pristine case as well as a few doped cases, whose results are presented in Fig. S2 within the SM [56]. We note that the spectra computed using the two functionals are qualitatively similar with the HSE06 spectrum being slightly blue-shifted with respect to the B3LYP one. Additionally, in Tables S3–S17 within the SM [56], we present detailed information regarding the TDDFT wave functions of the excited states contributing to various peaks of the optical absorption spectra computed using the B3LYP functional for all the QDs considered in this work.

1. Point-group symmetries

The point-group symmetries of the QDs considered in this work are D_{2h} , C_{2h} , C_{2v} , and C_s (see Table III), which we briefly discuss below.

The point-group symmetry of the pristine GQD (Fig. 1) is D_{2h} , and its closed-shell singlet ground state belongs to the irreducible representation (irrep) A_g , while the dipole-allowed excited states belong to irreps B_{1u} (z polarized), B_{2u} (y polarized), and B_{3u} (x polarized), respectively. Out of these, the excited states of B_{1u} irrep occur at much higher energy as compared to those of B_{2u} and B_{3u} ; therefore, we have ignored them in the present work. We note that with our choice of axes, long axis is along the y axis, while the short axis is along the x axis.

The BN-GQDs in which two separated BN rings are placed in such a manner that the inversion symmetry is obeyed, the point-group symmetry is C_{2h} . For these structures, the closed-shell ground state is of irrep A_g , while the dipole allowed excited states have the symmetries B_u , with the mixed xy polarization, and A_u with polarization along the z direction. As the z -polarized excitations occur at higher energies, we have only considered B_u symmetry excited states in the linear optical absorption spectra.

For those BN-GQDs in which the BN ring (rings) is (are) placed symmetrically, the point group is C_{2v} . The closed-shell ground state for such systems is of irrep A_1 , and because of the lack of inversion symmetry, x -polarized optical excitations are dipole allowed from the ground state to the excited states of irrep A_1 . The optical transitions to B_1 -type excited states are z -polarized (out of plane), while those to B_2 -type excited states are y polarized. Again, z -polarized optical transitions occur at much higher energies, so we have not probed B_1 -type excited states in this work.

C_s is the point-group symmetry of BN-GQDs in which the BN ring (rings) is (are) implanted in an asymmetric manner, with the mirror plane in the plane of the BN-GQD. This group has irreps A' and A'' , with the closed-shell ground state being of A' symmetry. The dipole transitions from the ground state to the excited states of the same A' symmetry have mixed xy polarization in the plane of the BN-GQDs, while those to the excited states of A'' symmetry are z -polarized. Similar to the previous cases, the z -polarized transitions occur at much higher energies, and, therefore, are not studied in this work.

2. Pristine GQD (dibenzo[bc,kl]coronene)

In Fig. 6, we present the linear optical absorption spectrum of the pristine GQD ($C_{30}H_{14}$), in which we indicate the polarization direction of the excited state contributing to each peak as a subscript of the peak label. We note the following trends: (a) There are four major peaks in the energy region (0.0–5.0 eV) explored in our calculations. (b) Peak I of the spectrum corresponding to the optical gap is long-axis polarized (B_{2u} irrep), and is located at 2.31 eV. The many-body wave function of the excited state contributing to this peak is dominated by HOMO (H) to LUMO (L) single excitation $|H \rightarrow L\rangle$. (c) Peak II of the spectrum at 3.46 eV is weaker in intensity compared to I, and is x -polarized (B_{3u}), with the excited state wave function dominated by the single excitation $|H - 2 \rightarrow L\rangle$. (d) The third peak at 4.08 eV has intensity similar to that of peak II, however, it is y -polarized. Its excited state wave function is dominated by the singly-excited configuration $|H - 1 \rightarrow L + 1\rangle$. (e) Peak IV located near 4.91 eV is the most intense (MI) peak of the spectrum, and is again y -polarized. It is due to two closely spaced excited states both of whose many-body wave functions are dominated by the single excitation $|H - 2 \rightarrow L + 2\rangle$. We note that the broad intensity profile, peak locations, and polarizations computed in this work are in excellent agreement with results of our earlier calculations on the same molecule (dibenzo[bc,kl]coronene), performed using the Pariser-Parr-Pople (PPP) model Hamiltonian [59]. Detailed information about the excited states contributing to the peaks are presented in Table S3 within the SM [56].

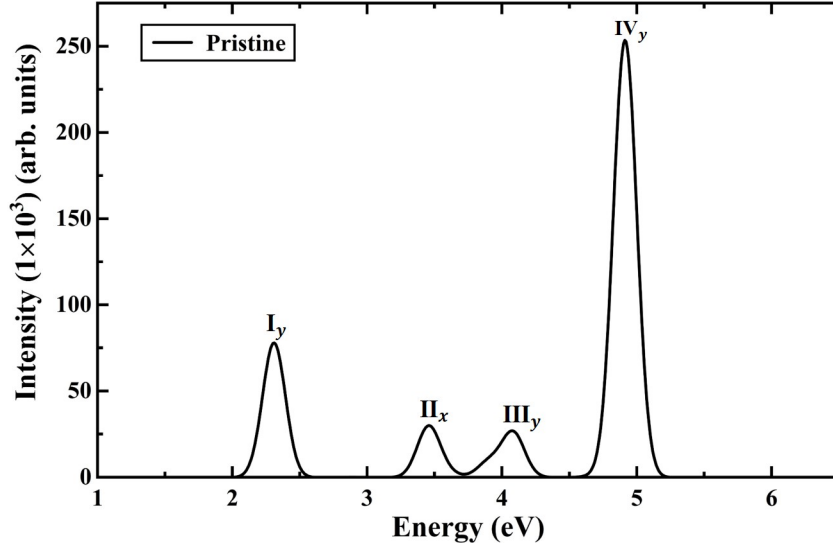


Figure 6. Optical absorption spectrum of pristine diamond shaped GQD, computed using the TDDFT approach, and B3LYP functional. The subscript of each peak label denotes polarization direction of the photon involved.

Next, we present and discuss the optical absorption spectra of various BN-GQDs to understand the influence of BN-ring doping on the optical response of the GQD.

3. Doping with single BN ring

In this category four different structures (models 1–4) are possible based on the BN-ring positions as shown in figure 2(a). These model BN-GQDs are isomers of each other with common chemical formula $C_{24}B_3N_3H_{14}$ of which the first two BN-GQDs (model 1, model 2) belong to the C_{2v} point group, while the other two (model 3, model 4) are of the C_s symmetry. The comparison between UV-Vis absorption spectra of these molecules with that of the pristine GQD, obtained using the TDDFT approach employing B3LYP functional is presented in Fig. S4 within the SM [56], while in Fig. 7 we present the absorption spectra of each BN-GQD, separately. Next, we briefly discuss the salient features of the absorption spectra of each of the four models. The detailed information relevant to the excited states of these BN-GQDs is presented in Tables S4–S7 within the SM [56].

Model 1:

In this model, the BN ring is placed right at the center of the GQD [see Fig. 2(a)], thereby reducing its symmetry to C_{2v} . The absorption spectrum of this BN-GQD is presented in Fig. 7(a), from which it is obvious that it has changed quite significantly as compared to that of the parent GQD. We note the following trends based on this figure and the information presented in Table S4 within the SM [56]. The location of peak I (the optical gap) gets blueshifted by about 0.2 eV compared to the pristine GQD. The MI peak is now peak II that is still y polarized similar to the parent GQD; however, it is comparatively redshifted by 1.4 eV. The wave function of this peak is dominated by the single excitation $|H - 1 \rightarrow L + 1\rangle$, similar to peak III of the parent GQD. The first intense x -polarized peak is now peak V located at 4.56 eV which is about 1.1 eV blueshifted as compared to the corresponding x -polarized peak (II) of the pristine GQD. The single excitation $|H - 1 \rightarrow L + 3\rangle$ makes dominant contribution to this peak of the BN-GQD, while peak II of the pristine GQD is mainly from the excitation $|H - 2 \rightarrow L\rangle$.

Model 2:

With the BN ring placed at the top corner of the GQD [see Fig. 2(a)], this BN-GQD is also C_{2v} symmetric. As compared to the absorption spectrum of the pristine GQD, model 2 exhibits a few extra peaks [see Fig. 7(b)]. As far as the first peak (peak I) is concerned, it is still y -polarized, but about 0.2 eV blueshifted as compared to the parent GQD, similar to model 1. Peak VI is now the MI peak which, however, has the same polarization (y) as the MI peak of the pristine GQD, and it is also blueshifted by a very small amount (0.05 eV) compared to the pristine one. Furthermore, similar to the parent GQD, the wave function of the MI peak in model 2 is dominated by the excitation $|H - 2 \rightarrow L + 2\rangle$. Compared to the pristine GQD which has a single x -polarized peak (II), in this model we obtain two significant x -polarized peaks (II and III), the first of which is redshifted compared to parent molecule while the second one (III) is blueshifted. Therefore, we conclude that the peaks II and III are a consequence of the splitting of peak II of the parent GQD because of the symmetry breaking. Along with x polarized transition, peak III also has contribution from a closely spaced y polarized transition. Because of the change in symmetry, different configurations

contribute to these x -polarized excited states in model 2 (see Table S5 within the SM [56]), as compared to the one in the pristine GQD.

Model 3:

In this model, the BN ring is placed at the right corner [see Fig. 2(a)] of the GQD; therefore, the resultant symmetry C_s is even lower than C_{2v} , leading to the mixed xy polarization of the transition dipole moments. When we compare the absorption spectrum of this model [see Fig. 7(c)], we note a general redshift of the spectral features as compared to the pristine GQD. The location of the first absorption peak is at 1.71 eV, which amounts to a redshift of 0.6 eV as compared to the parent molecule, although the wave functions contributing to the peak of both the molecules are still dominated by the $|H \rightarrow L\rangle$ transition. The MI peak (peak VII) of model 3 is about 0.3 eV redshifted as compared to that of the pristine GQD, while its wave function is dominated by the excitation $|H - 1 \rightarrow L + 3\rangle$. In addition to a couple of shoulders, there are three more (II, III, V) well-resolved peaks in the spectrum within the energy range 2.3–3.9 eV, owing to various other orbital excitations whose details are presented in Table S6 within the SM [56].

Model 4:

The BN-GQD of model 4 is obtained by placing the BN ring at one of the edges, which we chose to be the left-lower edge [Fig. 2(a)]. The symmetry of this BN-GQD is also C_s ; however, its absorption spectrum exhibits the most pronounced redistribution of the oscillator strength as compared to the pristine GQD, with the first peak becoming the MI peak. This peak (I) is owing to a state located at 2.09 eV which is about 0.2 eV redshifted compared to the optical gap of the pristine GQD, with the wave function dominated by the $|H \rightarrow L\rangle$ transition. Because the wave functions of peak I in model 4 is identical to that in the pristine GQD, this implies that it became the MI peak by redistribution of the oscillator strength and not due to the redshift of MI peak of the parent GQD. The other intense peaks [Fig. 7(d)] in the spectrum of this model are V, VII, and VIII located at 3.56 eV, 4.28 eV, and 4.85 eV, owing to the excited states described by the transitions $|H - 2 \rightarrow L\rangle$, $|H - 1 \rightarrow L + 2\rangle$, and $|H - 3 \rightarrow L + 1\rangle$, respectively. The detailed information about various

excited states in the spectrum of model 4 is presented in Table S7 within the SM [56].

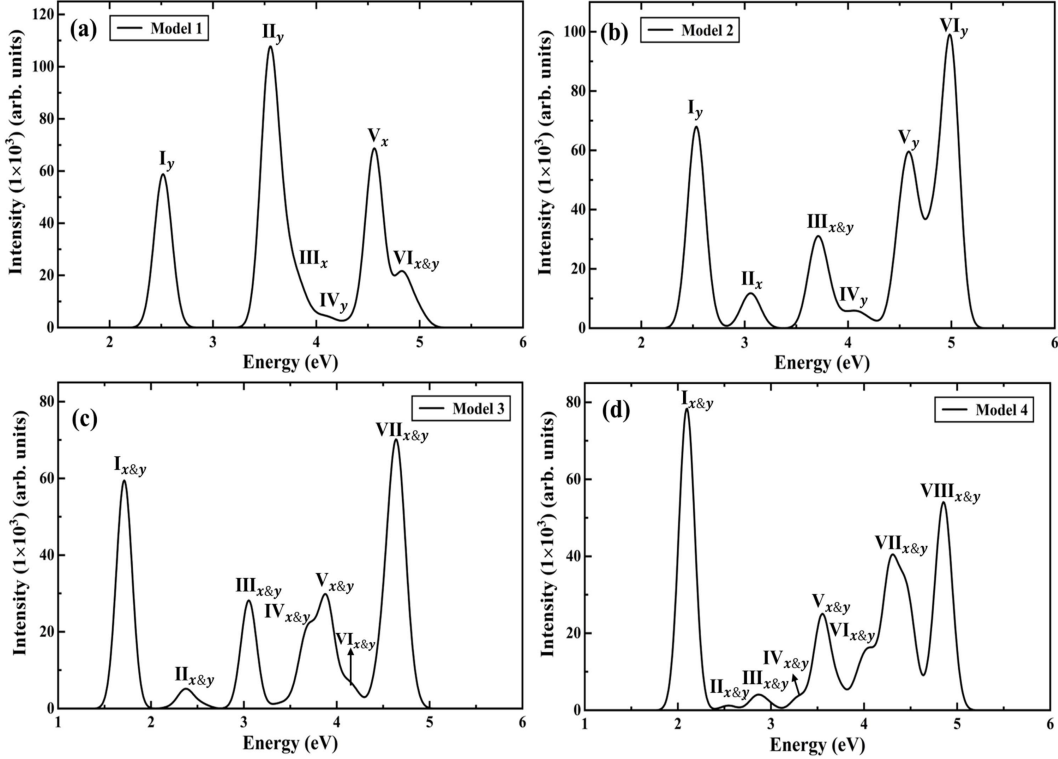


Figure 7. Linear optical absorption spectra for (a) Model 1, (b) Model 2, (c) Model 3, and (d) Model 4, computed at the TDDFT-B3LYP level of theory, assuming a uniform line width of 0.1 eV.

4. Doping with two fused BN rings

In Fig. 2(b), we depict four models (models 5–8) of BN-GQDs obtained by doping the parent GQD with two fused BN rings which are isomers with chemical formula $C_{20}B_5N_5H_{14}$. From the figure it is obvious that only model 7 has the C_{2v} symmetry, while the rest of them belong to the C_s point group. In Fig. S5 within the SM [56], we compare the absorption spectra of these molecules with that of the pristine GQD, obtained using the TDDFT approach, and the B3LYP functional, while in Fig. 8 we present the spectra of each BN-GQD, separately. The detailed information about the excited states contributing to the spectra of this class of BN-GQDs can be found in Tables S8–S11 within the SM [56]. Next, we briefly discuss the main characteristics of the absorption spectra of each of the four models.

Model 5:

As compared to the pristine GQD, the first peak of the spectrum of this model at 1.77 eV [Fig. 8(a)], exhibits a red shift of about 0.5 eV. Additionally, this peak is also the MI peak of this model, even though the excited state contributing to it is still dominated by $|H \rightarrow L\rangle$ excitation. This suggests a major redistribution of the oscillator strength similar to model 4. Additionally, this BN-GQD exhibits six more well-resolved peaks in the energy range 2.40–4.75 eV. From the peak locations of this BN-GQD as listed in Table S8 within the SM [56], it is obvious that as compared to the parent GQD, the entire spectrum is red shifted. The second most intense peak [peak VIII of Fig. 8(a)] of this model is located at 4.75 eV and is owing to two closely spaced excited states whose wave functions are dominated by excitations $|H - 6 \rightarrow L\rangle$ and $|H - 1 \rightarrow L + 4\rangle$.

Model 6:

As compared to the pristine GQD, in this model the first peak [peak I of Fig. 8(b)] undergoes a slight blue shift of 0.1 eV, however, the MI peak (peak IV) gets red shifted by about 1.1 eV to the position 3.78 eV, and is dominated by the excitation $|H - 1 \rightarrow L + 1\rangle$ (see Table S9 within the SM [56]). We note that for the pristine GQD, peak III located near 4.1 eV is also dominated by the $|H - 1 \rightarrow L + 1\rangle$ excitation, even though it is not the MI peak. This indicates redistribution of the oscillator strength in this BN-GQD caused by doping.

Model 7:

Even though this model is C_{2v} symmetric, as compared to the pristine GQD, it exhibits a significant redshift of about 1.1 eV, from 2.31 eV to 1.17 eV, in the location of the first peak, amounting to about 50% reduction. Despite this, the y -polarization [Fig. 8(c)] of the peak remains unchanged as also the nature of the excited state with the dominant $|H \rightarrow L\rangle$ excitation (see Table S10 within the SM [56]). The MI peak (peak VII) in this model is also y -polarized similar to the MI peak of the pristine GQD, although it occurs at 4.32 eV, which is comparatively 0.6 eV red shifted. Additionally, there are several well-resolved peaks in the energy region between the optical gap and the MI peak.

Model 8:

This C_s -symmetric model is obtained by replacing the two carbon hexagons in the central row of the parent GQD by two fused BN rings, leading to a very prominent red shift in the absorption spectrum [see Fig. 8(d)]. The first peak (peak I) of this BN-GQD is located at 1.23 eV which is also about 1.1 eV lower than the first peak of the parent GQD at 2.31 eV. However, the relative intensity of peak I, as compared to the first peaks of other three fused double-ring doped models, is significantly lower. Peak III located at 2.93 eV is the MI peak of this model, and as compared to the pristine GQD it is red shifted by almost about 2 eV. The transition contributing most to this peak is $|H - 1 \rightarrow L + 1\rangle$, which is similar to peak III of the pristine GQD located at 4.08 eV. Additionally, there are several smaller peaks in the computed spectrum of this GQD that are quite well resolved. The detailed information about various excited states in the spectrum of this model is presented in Table S11 within the SM [56].

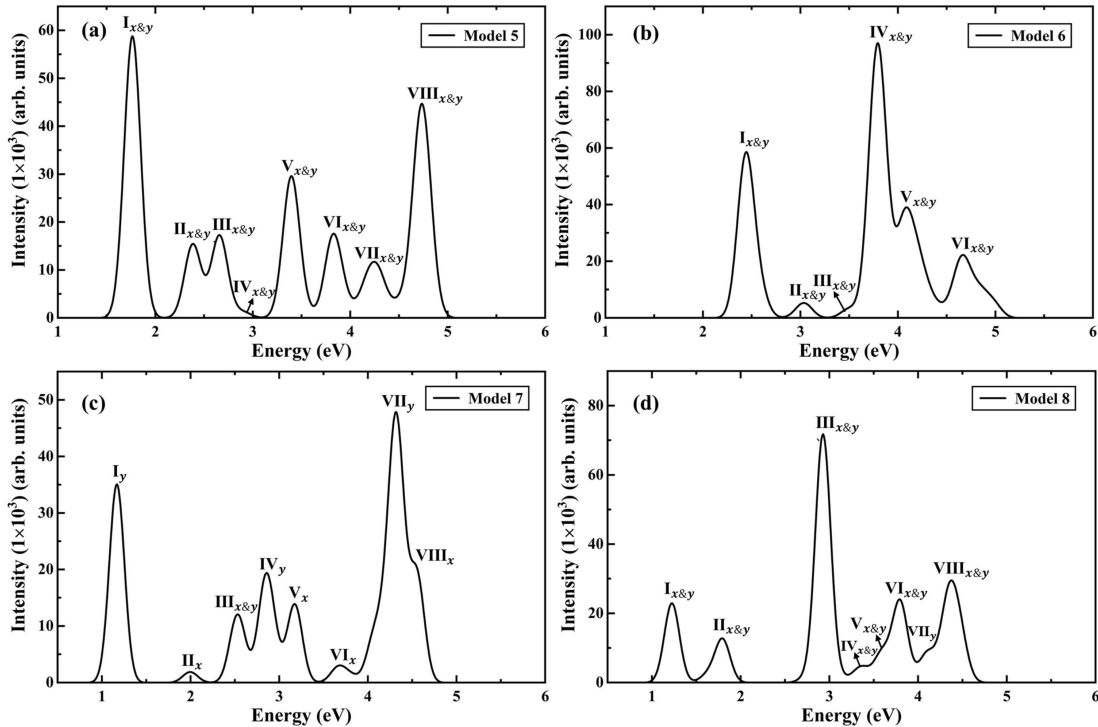


Figure 8. Linear optical absorption spectra for (a) Model 5, (b) Model 6, (c) Model 7, and (d) Model 8, computed at the TDDFT-B3LYP level of theory, assuming a uniform line width of 0.1 eV.

5. Doping with two separated BN rings

BN-GQDs of this category are obtained by replacing two separated carbon hexagons in the pristine GQD by two B_3N_3 hexagons as shown in Fig. 2(c). As a result, all the BN-GQDs in this class are isomeric with the chemical formula $C_{18}B_6N_6H_{14}$. As the two rings are separated, we have more freedom in this case as compared to the previous one because we can orient the two hexagons in a parallel ($\uparrow - \uparrow$) or antiparallel ($\uparrow - \downarrow$) manner. We have considered three possible arrangements of the separated BN rings; however, combined with their relative orientations, we get twice the number, i.e., six BN-GQDs from them. As is shown in Table III, these six models have symmetries ranging from high (D_{2h}) to low (C_s). The UV-Vis spectra for all the models of this class are compared to that of the pristine GQD in Fig. S6 within the SM [56], while for the individual BN-GQDs they are presented in Figs. 9(a)–(f). Furthermore, in Tables S12–S17 within the SM [56] all the details regarding the excited states contributing to the spectra of each BN-GQD of this class are presented. Next, we briefly discuss the main features of their absorption spectra.

Model 9:

This model is obtained by substituting BN rings on the top and bottom corners of the pristine GQD, and when we choose the parallel orientation the point group of the BN-GQD is C_{2v} , while for the antiparallel orientation it is D_{2h} . We note that for both the orientations the first peak is y polarized [see Figs. 9(a) and (d)] and blue shifted with respect to the first peak of the parent GQD by more than 0.4 eV. For the parallel orientation [Fig. 9(a)], there are two almost equal intensity y -polarized peaks, III (4.0 eV) and V (4.8 eV) which qualify as the MI peaks. We note that as compared to the MI peak of the pristine GQD at 4.9 eV, peak III is red shifted, while peak V is almost unchanged. In this case also, as compared to the parent GQD, there is a significant transfer of oscillator strength from peak IV to peak III, because both the polarization and orbital excitations contributing to the peaks III ($|H - 1 \rightarrow L + 1\rangle$) and V ($|H - 2 \rightarrow L + 2\rangle$) of this BN-GQD are the same as for the peaks III and IV of pristine GQD. For the antiparallel orientation [Fig. 9(d)], there is a single y -polarized MI peak (II) located at 4.06 eV which is about 0.8 eV red shifted with respect to that in the pristine GQD. The detailed information about the excited states for

the two BN-GQDs of this class is presented in Tables S12 and S13 within the SM [56].

Model 10:

To obtain this model, one substitutes the two separated BN rings in the middle row of the parent GQD, and for the parallel orientation the point group of the BN-GQD is C_{2v} , while for the antiparallel orientation it is C_{2h} . The spectra of both the BN-GQDs of this class are significantly red shifted as compared to the parent GQD, as it is obvious from Figs. 9(b) and (e). Peak I for the parallel and antiparallel orientations occur at 1.27 eV and 1.46 eV, respectively, both of which are significantly red shifted compared to the corresponding peak in the pristine GQD at 2.31 eV. As far as the MI peaks are concerned, for the parallel orientation two peaks I (y polarized) and IV (x polarized at 2.86 eV) will qualify; however, for the antiparallel orientation peak I is also the MI peak. Additionally, in both the spectra there are several well-resolved peaks in the energy range 2–4.5 eV. Wave functions for the first peaks of both the BN-GQDs are dominated by the $|H \rightarrow L\rangle$ excitation, while the x -polarized peak IV for the parallel orientation derives main contribution from the $|H-2 \rightarrow L\rangle$ transition. The detailed information about the excited states for the two BN-GQDs of this class is presented in Tables S14 and S15 within the SM [56].

Model 11:

In this model, the BN rings are placed along a diagonal of the GQD, which for the parallel orientation corresponds to the C_s point group, while for the antiparallel orientation the point group is C_{2h} . For the parallel and anti-parallel orientations, the computed spectra are presented in Figs. 9(c) and (f), respectively, while the detailed information about the excited states contributing to the spectra is given in Tables S16 and S17 within the SM [56]. The location of peak I of the parallel orientation is at 1.59 eV, while that for the antiparallel case is 1.73 eV, both of which are quite red shifted compared to peak I of the pristine GQD. For the parallel orientation, in addition to peak I, peaks IV (3.33 eV) and VII (4.29 eV) also carry large intensities, although peak VII is the MI peak. For the antiparallel orientation, peak I is the MI peak, while peaks IV (3.42 eV), V (4.11 eV), and VI (4.61 eV) also have significant intensities. Thus, broadly speaking, most of the features of these BN-GQDs are

red shifted as compared to the parent GQD, although not to the extent as in model 10.

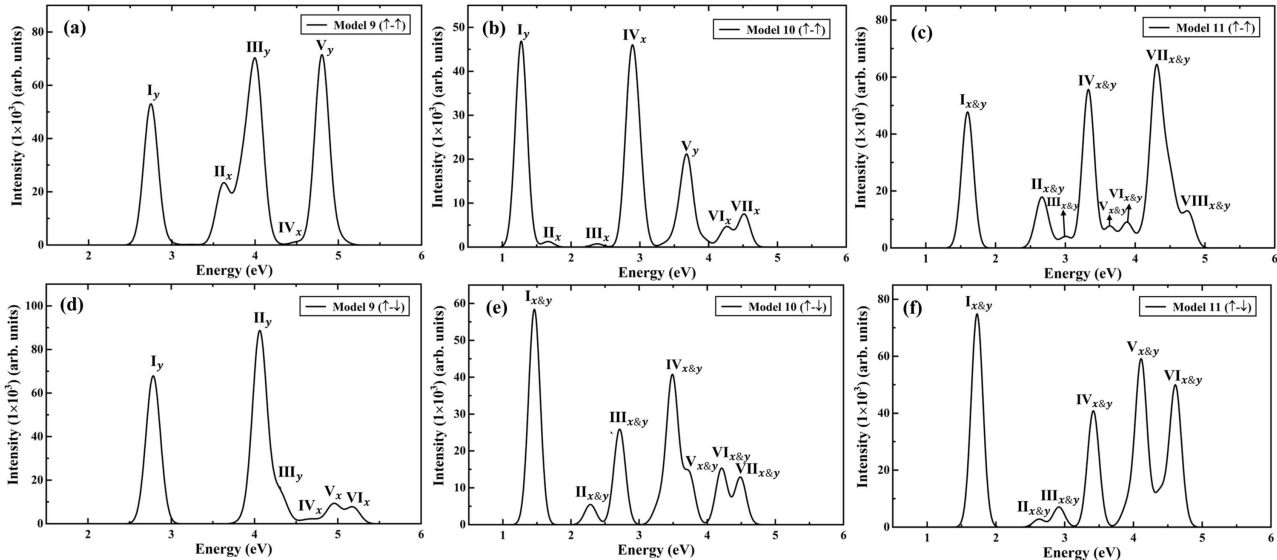


Figure 9. Linear optical absorption spectra for (a) Model 9 ($\uparrow - \uparrow$), (b) Model 10 ($\uparrow - \uparrow$), (c) Model 11 ($\uparrow - \uparrow$), (d) Model 9 ($\uparrow - \downarrow$), (e) Model 10 ($\uparrow - \downarrow$), and (f) Model 11 ($\uparrow - \downarrow$), computed at the TDDFT-B3LYP level of theory, assuming a uniform line width of 0.1 eV.

6. Summary of the absorption spectra

We note the following trends in the optical gaps and the absorption spectra of the doped structures, as compared to the pristine GQD: (a) Out of the fourteen doped structures considered, the optical gaps of five models increase as compared to the pristine GQD, while for nine cases the gaps decrease. (b) The point-group symmetry of the doped structure is not a good descriptor of the shifts in the optical gaps or in the intensity profiles of the absorption spectra. For example, model 9 ($\uparrow - \uparrow$) with C_{2v} symmetry exhibits a blue shift in the optical gap, while model 10 ($\uparrow - \uparrow$) also with C_{2v} symmetry undergoes a significant red shift. (c) As discussed previously, the redistribution of the charge associated with the HOMO/LUMO of the doped structures, as compared to those of the pristine GQD, appears to describe the changes in the optical gaps to a reasonable extent. (d) The locations of the dopant $(\text{BN})_3$ rings have a strong impact on the nature of the corresponding absorption spectra. For example, models 1 and 2 have the same point group symmetry (C_{2v}), and almost identical optical gaps, but their absorption spectra are quite different from each other because of the

different locations of the dopant rings. (e) For the cases of doping with two separated $(\text{BN})_3$ rings (models 9, 10, and 11), for a given model, the relative orientations of the rings ($\uparrow - \uparrow$ vs $\uparrow - \downarrow$) impact their absorption spectra significantly (see Fig. 9). Thus, we conclude that the different doping models have significantly different electronic structures as compared to each other, leading to distinct optical absorption spectra.

IV. CONCLUSIONS

In this work we considered a highly symmetric diamond-shaped GQD with the D_{2h} point group symmetry, and replaced up to two carbon hexagons in it with B_3N_3 hexagonal rings at various places to obtain different BN-ring doped structures. Depending on the placement of BN rings, the resultant structures have point groups ranging from the high-symmetry D_{2h} to the lowest symmetry C_s . All the BN-ring doped GQDs considered in this study are dynamically and energetically stable. We found that even after BN ring doping, the resultant structures continue to be planar, leading to $\sigma - \pi$ separation. The orbital analysis and DOS calculations both reveal that the occupied and the unoccupied orbitals close to the Fermi level continue to be of π and π^* type, respectively, just as in case of the parent GQD. Subsequently, we computed their linear UV-Vis absorption spectra, and found that they are dominated by $\pi - \pi^*$ transitions. Furthermore, we found that by choosing suitable doping configurations, one can tune the optical gaps of the BN-GQDs considered in this work in a wide frequency range, spanning infrared to visible. This property makes the considered doping strategy, and the resultant BN-GQDs potentially quite useful in optoelectronic applications. Therefore, we hope that our results will motivate the experimentalists to synthesize these nanostructures and study their optical properties.

Because the low-lying optical excitations in these structures are of $\pi - \pi^*$ type, we plan to parametrize the Pariser-Parr-Pople (PPP) model Hamiltonian for these systems, which is normally used for the organic π -conjugated molecules. This will significantly reduce the number of degrees of freedom, allowing the exploration of much larger BN-doped, or BN-based, planar systems employing higher level quantum many-body approaches. Furthermore, a majority of the doped structures considered in this work lacked the inversion symmetry; therefore, they will also exhibit second-order nonlinear optical response. Investigations along these directions are currently underway in our group, and the results will be communicated

in future publications.

DATA AVAILABILITY

The majority of the data are given in the main article and the Supplemental Material. The rest of the data will be available from the authors upon reasonable request.

-
- [1] C.-B. Ma, Z.-T. Zhu, H.-X. Wang, X. Huang, X. Zhang, X. Qi, H.-L. Zhang, Y. Zhu, X. Deng, Y. Peng, *et al.*, A general solid-state synthesis of chemically-doped fluorescent graphene quantum dots for bioimaging and optoelectronic applications, *Nanoscale* **7**, 10162 (2015).
 - [2] W. Zuo, L. Tang, J. Xiang, R. Ji, L. Luo, L. Rogée, and S. Ping Lau, Functionalization of graphene quantum dots by fluorine: Preparation, properties, application, and their mechanisms, *Applied Physics Letters* **110** (2017).
 - [3] G. Yang, C. Wu, X. Luo, X. Liu, Y. Gao, P. Wu, C. Cai, and S. S. Saavedra, Exploring the emissive states of heteroatom-doped graphene quantum dots, *The Journal of Physical Chemistry C* **122**, 6483 (2018).
 - [4] K. S. Novoselov, A. K. Geim, S. V. Morozov, D. Jiang, Y. Zhang, S. V. Dubonos, I. V. Grigorieva, and A. A. Firsov, Electric field effect in atomically thin carbon films, *Science* **306**, 666 (2004).
 - [5] A. E. Galashev and O. R. Rakhmanova, Mechanical and thermal stability of graphene and graphene-based materials, *Physics-Uspekhi* **57**, 970 (2014).
 - [6] M. Liu, X. Yin, E. Ulin-Avila, B. Geng, T. Zentgraf, L. Ju, F. Wang, and X. Zhang, A graphene-based broadband optical modulator, *Nature* **474**, 64 (2011).
 - [7] A. Singh, M. Uddin, J. Tolson, H. Maire-Afeli, N. Sbrockey, G. Tompa, M. Spencer, T. Vogt, T. Sudarshan, and G. Koley, Electrically tunable molecular doping of graphene, *Applied Physics Letters* **102** (2013).
 - [8] J. Cai, P. Ruffieux, R. Jaafar, M. Bieri, T. Braun, S. Blankenburg, M. Muoth, A. P. Seitsonen, M. Saleh, X. Feng, *et al.*, Atomically precise bottom-up fabrication of graphene nanoribbons, *Nature* **466**, 470 (2010).

- [9] L. Jiao, X. Wang, G. Diankov, H. Wang, and H. Dai, Facile synthesis of high-quality graphene nanoribbons, *Nature Nanotechnology* **5**, 321 (2010).
- [10] L.-s. Li and X. Yan, Colloidal graphene quantum dots, *The Journal of Physical Chemistry Letters* **1**, 2572 (2010).
- [11] X. Huang, Z. Yin, S. Wu, X. Qi, Q. He, Q. Zhang, Q. Yan, F. Boey, and H. Zhang, Graphene-based materials: synthesis, characterization, properties, and applications, *Small* **7**, 1876 (2011).
- [12] M. Bacon, S. J. Bradley, and T. Nann, Graphene quantum dots, *Particle & Particle Systems Characterization* **31**, 415 (2014).
- [13] S. Kim, S. W. Hwang, M.-K. Kim, D. Y. Shin, D. H. Shin, C. O. Kim, S. B. Yang, J. H. Park, E. Hwang, S.-H. Choi, *et al.*, Anomalous behaviors of visible luminescence from graphene quantum dots: interplay between size and shape, *ACS Nano* **6**, 8203 (2012).
- [14] B. Geffroy, P. Le Roy, and C. Prat, Organic light-emitting diode (OLED) technology: materials, devices and display technologies, *Polymer International* **55**, 572 (2006).
- [15] H.-W. Chen, J.-H. Lee, B.-Y. Lin, S. Chen, and S.-T. Wu, Liquid crystal display and organic light-emitting diode display: present status and future perspectives, *Light: Science & Applications* **7**, 17168 (2018).
- [16] Y. Liu, C. Li, Z. Ren, S. Yan, and M. R. Bryce, All-organic thermally activated delayed fluorescence materials for organic light-emitting diodes, *Nature Reviews Materials* **3**, 1 (2018).
- [17] A. Facchetti, π -conjugated polymers for organic electronics and photovoltaic cell applications, *Chemistry of Materials* **23**, 733 (2011).
- [18] Z. Zhu, J. Ma, Z. Wang, C. Mu, Z. Fan, L. Du, Y. Bai, L. Fan, H. Yan, D. L. Phillips, *et al.*, Efficiency enhancement of perovskite solar cells through fast electron extraction: the role of graphene quantum dots, *Journal of the American Chemical Society* **136**, 3760 (2014).
- [19] C. Wang, H. Dong, W. Hu, Y. Liu, and D. Zhu, Semiconducting π -conjugated systems in field-effect transistors: a material odyssey of organic electronics, *Chemical Reviews* **112**, 2208 (2012).
- [20] H. Sirringhaus, Organic field-effect transistors: the path beyond amorphous silicon, *Advanced Materials* **26**, 1319 (2014).
- [21] B. Lussem, C.-M. Keum, D. Kasemann, B. Naab, Z. Bao, and K. Leo, Doped organic transistors, *Chemical Reviews* **116**, 13714 (2016).

- [22] T. Wehling, K. Novoselov, S. Morozov, E. Vdovin, M. Katsnelson, A. Geim, and A. Lichtenstein, Molecular doping of graphene, *Nano Letters* **8**, 173 (2008).
- [23] H. Liu, Y. Liu, and D. Zhu, Chemical doping of graphene, *Journal of Materials Chemistry* **21**, 3335 (2011).
- [24] S. Kawai, S. Saito, S. Osumi, S. Yamaguchi, A. S. Foster, P. Spijker, and E. Meyer, Atomically controlled substitutional boron-doping of graphene nanoribbons, *Nature Communications* **6**, 8098 (2015).
- [25] B. Xu, Y. Lu, Y. Feng, and J. Lin, Density functional theory study of BN-doped graphene superlattice: role of geometrical shape and size, *Journal of Applied Physics* **108** (2010).
- [26] F. N. Ajeel, M. N. Mutier, K. H. Mohsin, S. K. Khamees, A. M. Khudhair, and A. B. Ahmed, Theoretical study on electronic properties of BN dimers doped graphene quantum dots, *Bio-NanoScience* **14**, 1110 (2024).
- [27] H. Fei, R. Ye, G. Ye, Y. Gong, Z. Peng, X. Fan, E. L. Samuel, P. M. Ajayan, and J. M. Tour, Boron-and nitrogen-doped graphene quantum dots/graphene hybrid nanoplatelets as efficient electrocatalysts for oxygen reduction, *ACS Nano* **8**, 10837 (2014).
- [28] R. S. Li, B. Yuan, J. H. Liu, M. L. Liu, P. F. Gao, Y. F. Li, M. Li, and C. Z. Huang, Boron and nitrogen co-doped single-layered graphene quantum dots: a high-affinity platform for visualizing the dynamic invasion of HIV DNA into living cells through fluorescence resonance energy transfer, *J. Mater. Chem. B* **5**, 8719 (2017).
- [29] P. Yang, J. Su, R. Guo, F. Yao, and C. Yuan, B,N-co-doped graphene quantum dots as fluorescence sensor for detection of Hg^{2+} and F^- ions, *Anal. Methods* **11**, 1879 (2019).
- [30] E. Budak and C. Ünlü, Boron regulated dual emission in B, N doped graphene quantum dots, *Optical Materials* **111**, 110577 (2021).
- [31] X. Chen, D. Tan, and D.-T. Yang, Multiple-boron-nitrogen (multi-BN) doped π -conjugated systems for optoelectronics, *J. Mater. Chem. C* **10**, 13499 (2022).
- [32] C. Sánchez-Sánchez, S. Brüller, H. Sachdev, K. Müllen, M. Krieg, H. F. Bettinger, A. Nicolai, V. Meunier, L. Talirz, R. Fasel, and P. Ruffieux, On-surface synthesis of BN-substituted heteroaromatic networks, *ACS Nano* **9**, 9228 (2015).
- [33] C. Chen, K. Guo, Y. Zhu, F. Wang, W. Zhang, and H. Qi, Construction of layered B₃N₃-doped graphene sheets from an acetylenic compound containing B₃N₃ by a semisynthetic strategy, *ACS Applied Materials & Interfaces* **11**, 33245 (2019).

- [34] N. Herrera-Reinoza, A. C. dos Santos, L. H. de Lima, R. Landers, and A. de Siervo, Atomically precise bottom-up synthesis of h-BNC: graphene doped with h-BN nanoclusters, *Chemistry of Materials* **33**, 2871 (2021).
- [35] L. Caputo, V.-H. Nguyen, and J.-C. Charlier, First-principles study of the structural and electronic properties of BN-ring doped graphene, *Phys. Rev. Mater.* **6**, 114001 (2022).
- [36] C. Nguyen, N. V. Hoang, H. V. Phuc, A. Y. Sin, and C. V. Nguyen, Two-dimensional boron phosphide/MoGe₂N₄ van der Waals heterostructure: A promising tunable optoelectronic material, *The Journal of Physical Chemistry Letters* **12**, 5076 (2021).
- [37] C. V. Nguyen, P. T. Truong, H. V. Phuc, C. Q. Nguyen, N. T. Hiep, and N. N. Hieu, Rationally designed versatile heterostructures consisted of two-dimensional Goldene and MXene Sc₂CF₂, *Nano Letters* **25**, 10673 (2025).
- [38] P. T. Truong, N. N. Hieu, H. V. Nguyen, C. Q. Nguyen, T. P. T. Linh, H. V. Phuc, and C. V. Nguyen, Electronic properties and interfacial engineering of metal-semiconductor 1T-, 2H-Ta₂B MBene/Janus MoSSe heterostructures, *Nanoscale* **17**, 17182 (2025).
- [39] M. J. Frisch, G. W. Trucks, H. B. Schlegel, G. E. Scuseria, M. A. Robb, J. R. Cheeseman, G. Scalmani, V. Barone, G. A. Petersson, *et al.*, Gaussian 16, Revision C.01 (2016), Gaussian, Inc., Wallingford CT.
- [40] C. Lee, W. Yang, and R. G. Parr, Development of the Colle-Salvetti correlation-energy formula into a functional of the electron density, *Physical review B* **37**, 785 (1988).
- [41] A. D. Becke, Density-functional thermochemistry. I. The effect of the exchange-only gradient correction, *The Journal of Chemical Physics* **96**, 2155 (1992).
- [42] A. Becke, Density-Functional Thermochemistry. III. The Role of Exact Exchange. *J. Chem. Phys.*, 98: 5648-5652 (1993).
- [43] E. Runge and E. K. U. Gross, Density-functional theory for time-dependent systems, *Phys. Rev. Lett.* **52**, 997 (1984).
- [44] M. Marques and E. Gross, Time-dependent density functional theory, *Annual Review of Physical Chemistry* **55**, 427 (2004).
- [45] W. J. Hehre, R. Ditchfield, and J. A. Pople, Self-consistent molecular orbital methods. XII. Further extensions of Gaussian-type basis sets for use in molecular orbital studies of organic molecules, *The Journal of Chemical Physics* **56**, 2257 (1972).

- [46] P. C. Hariharan and J. A. Pople, The influence of polarization functions on molecular orbital hydrogenation energies, *Theoretica Chimica Acta* **28**, 213 (1973).
- [47] W. Kohn and L. J. Sham, Self-consistent equations including exchange and correlation effects, *Physical Review* **140**, A1133 (1965).
- [48] R. Bauernschmitt and R. Ahlrichs, Treatment of electronic excitations within the adiabatic approximation of time dependent density functional theory, *Chemical Physics Letters* **256**, 454 (1996).
- [49] G. Scalmani, M. J. Frisch, B. Mennucci, J. Tomasi, R. Cammi, and V. Barone, Geometries and properties of excited states in the gas phase and in solution: Theory and application of a time-dependent density functional theory polarizable continuum model, *The Journal of Chemical Physics* **124** (2006).
- [50] F. Furche and R. Ahlrichs, Adiabatic time-dependent density functional methods for excited state properties, *The Journal of Chemical Physics* **117**, 7433 (2002).
- [51] Geometric derivatives of excitation energies using SCF and DFT, *Chemical Physics Letters* **308**, 249 (1999).
- [52] Geometric derivatives of density functional theory excitation energies using gradient-corrected functionals, *Chemical Physics Letters* **317**, 159 (2000).
- [53] R. E. Stratmann, G. E. Scuseria, and M. J. Frisch, An efficient implementation of time-dependent density-functional theory for the calculation of excitation energies of large molecules, *The Journal of Chemical Physics* **109**, 8218 (1998).
- [54] M. E. Casida, C. Jamorski, K. C. Casida, and D. R. Salahub, Molecular excitation energies to high-lying bound states from time-dependent density-functional response theory: Characterization and correction of the time-dependent local density approximation ionization threshold, *The Journal of Chemical Physics* **108**, 4439 (1998).
- [55] S. Das and A. Shukla, DFT and model hamiltonian study of optoelectronic properties of some low-symmetry graphene quantum dots, *The Journal of Physical Chemistry A* **128**, 10099 (2024).
- [56] See Supplemental Material for optimized geometry parameters, information about the excited states contributing to the peaks in the calculated absorption spectra, orbital projected DOS plots, comparison of absorption spectra computed using the B3LYP and HSE06 functionals, UV-Vis absorption spectra computed using different number of excited states and UV-Vis

spectra computed for various doping models compared to that of pristine GQD.

- [57] T. Lu and F. Chen, Multiwfn: A multifunctional wavefunction analyzer, *Journal of Computational Chemistry* **33**, 580 (2012).
- [58] E. Clar and W. Schmidt, Correlations between photoelectron and ultraviolet absorption spectra of polycyclic hydrocarbons: The terylene and peropyrene series, *Tetrahedron* **34**, 3219 (1978).
- [59] T. Basak, H. Chakraborty, and A. Shukla, Theory of linear optical absorption in diamond-shaped graphene quantum dots, *Phys. Rev. B* **92**, 205404 (2015).

Supplemental Material for “Tuning the optoelectronic properties of graphene quantum dots by BN-ring doping: A density functional theory study”

Samayita Das^{1,*} and Alok Shukla^{1,†}

¹*Department of Physics, Indian Institute of Technology Bombay, Powai, Mumbai 400076, India*

In this Supplemental Material (SM), Tables S1 and S2 represent the optimized bond lengths and bond angles, respectively, showing the minima and maxima for all the doped structures considered.

Next, Tables S3–S17 contain the information regarding the excited states contributing to important peaks in the calculated absorption spectra of the pristine and the BN-GQDs considered in this work. This includes peak positions E , symmetries of the excited states contributing to various peaks, oscillator strengths f , polarization direction of the absorbed photon indicated by the subscripts in the ‘Peak’ column, and the many-body wave functions of the excited states. Here, $f (= \frac{2 \times m_e}{3 \times \hbar^2} (E) \sum_{j=x,y,z} |\langle e | O_j | r \rangle|^2)$ indicates the oscillator strength for a particular transition where E , $|e\rangle$, $|r\rangle$, and O_j are representing the peak energy, excited states of the corresponding peak, reference state, and the Cartesian components of the electric dipole operator, respectively. In the last column, the numbers inside the parentheses represent the contributing coefficients of the wave functions for each corresponding configuration.

This SM also contains several figures depicting: the total and orbital projected density of states (Fig. S1), UV-Vis absorption spectra computed using the B3LYP and HSE06 functionals (Fig. S2), UV-Vis absorption spectra computed using different numbers of excited states (Fig. S3), and UV-Vis absorption spectra computed for various doping models compared to that of the pristine GQD (Figs. S4–S6).

A. Optimized Geometry Parameters

Table S1. Optimized bond lengths for the fourteen doped structures.

BN-ring doped structures	(C – C)Å (Min - Max)	(B – N)Å (Min - Max)	(C – B)Å (Min - Max)	(C – N)Å (Min - Max)	(C – H)Å (Min - Max)	(N – H)Å (Min - Max)	(B – H)Å (Min - Max)
Model 1	1.399 – 1.440	1.437 – 1.450	1.497 – 1.522	1.396 – 1.410	1.085 – 1.091	–	–
Model 2	1.379 – 1.462	1.409 – 1.426	1.517	1.396	1.086 – 1.090	1.011	1.194
Model 3	1.357 – 1.445	1.399 – 1.470	1.484 – 1.499	1.357 – 1.401	1.086 – 1.089	1.012	1.193
Model 4	1.375 – 1.447	1.425 – 1.457	1.491 – 1.516	1.384 – 1.410	1.085 – 1.090	–	1.192
Model 5	1.354 – 1.445	1.404 – 1.476	1.491 – 1.516	1.383 – 1.399	1.085 – 1.090	1.011	1.191 – 1.193
Model 6	1.353 – 1.427	1.430 – 1.450	1.499 – 1.532	1.385 – 1.410	1.084 – 1.093	–	1.192
Model 7	1.357 – 1.436	1.405 – 1.451	1.496 – 1.497	1.369 – 1.411	1.083 – 1.093	–	1.192 – 1.193
Model 8	1.363 – 1.442	1.396 – 1.483	1.494 – 1.525	1.345 – 1.411	1.085 – 1.090	1.013	1.193
Model 9 (↑ – ↑)	1.354 – 1.457	1.426 – 1.471	1.499 – 1.519	1.391	1.086 – 1.090	1.011	1.192 – 1.195
Model 9 (↑ – ↓)	1.345 – 1.467	1.425 – 1.463	1.515 – 1.516	1.404	1.087 – 1.089	1.011	1.194
Model 10 (↑ – ↑)	1.390 – 1.460	1.399 – 1.472	1.480 – 1.482	1.361 – 1.408	1.086 – 1.089	1.012	1.193
Model 10 (↑ – ↓)	1.392 – 1.456	1.399 – 1475	1.491 – 1.524	1.354 – 1.396	1.086 – 1.089	1.012	1.193
Model 11 (↑ – ↑)	1.359 – 1.453	1.414 – 1.488	1.459 – 1.533	1.371 – 1.414	1.085 – 1.090	1.012	1.191
Model 11 (↑ – ↓)	1.357 – 1.455	1.419 – 1.474	1.514 – 1.539	1.378 – 1399	1.085 – 1.090	1.012	–

* samayitadas5@gmail.com

† shukla@iitb.ac.in

Table S2. Optimized bond angles for the fourteen doped structures.

BN-ring doped structures	$\angle C - B - N$ ($^\circ$) (Min - Max)	$\angle B - N - B$ ($^\circ$) (Min - Max)	$\angle N - B - N$ ($^\circ$) (Min - Max)	$\angle C - C - C$ ($^\circ$) (Min - Max)	$\angle C - N - B$ ($^\circ$) (Min - Max)	$\angle C - C - B$ ($^\circ$) (Min - Max)	$\angle C - C - N$ ($^\circ$) (Min - Max)
Model 1	120.05 – 120.42	120.43 – 120.44	119.39 – 119.91	119.79 – 121.80	118.91 – 120.6	117.04 – 118.78	119.91 – 120.71
Model 2	118	118.7 – 122	118.44	118.6 – 122	120.6	119.6	120.24
Model 3	118.35 – 120.31	119.42 – 119.68	117 – 121.8	119.47 – 121.26	119.07 – 119.17	119.13 – 119.83	119.64 – 121
Model 4	119.44 – 120.23	119.29 – 121.48	118 – 120.3	118.12 – 120.3	117.5 – 120.47	117.15 – 120	118.86 – 122
Model 5	118 – 120.48	119.34 – 121.6	118 – 121.48	118.74 – 121.6	119.51 – 120.22	117.47 – 119.50	118.98 – 120.42
Model 6	119.24 – 121.44	119.27 – 121.95	119 – 120.74	119 – 121.69	118.92 – 121.6	118.60 – 119.86	118.1 – 122
Model 7	120.3 – 120.99	119.85 – 121.38	118.77 – 119.75	119.42 – 121.34	117.86 – 118	119.54 – 120.95	120.52 – 122
Model 8	119.59 – 120.32	118.8 – 120.89	119.1 – 121.14	119.43 – 120.27	118.94 – 121.13	118 – 121.15	118.22 – 120.90
Model 9 ($\uparrow - \uparrow$)	118.7 – 119.6	119.27 – 120	181 – 120.87	119.5 – 121	118 – 120.36	119.5 – 120	119.96 – 120.01
Model 9 ($\uparrow - \downarrow$)	118.3	118.8 – 122	118.96 – 119.02	119.45 – 121	120.91 – 120.96	119.72	120.52
Model 10 ($\uparrow - \uparrow$)	118.6 – 119	119.26 – 122.3	117 – 122	119 – 120.7	118.8 – 120.74	119 – 121.5	120.1 – 122
Model 10 ($\uparrow - \downarrow$)	118 – 121.6	120.15 – 121.99	118 – 119.63	119.6 – 121.13	119.38 – 120.42	119.34 – 119.7	120.95 – 122
Model 11 ($\uparrow - \uparrow$)	118.79 – 120.37	118 – 122	118 – 122.03	119.98 – 121.85	118.4 – 121.68	118 – 121.65	119.1 – 122
Model 11 ($\uparrow - \downarrow$)	118.1 – 120.25	120.34 – 122	117 – 120.6	119 – 121.53	119.32 – 120.06	118 – 119.1	119.96 – 120.98

B. Data from the TDDFT calculations of the UV-Vis absorption spectra

The wave function analysis of the different peaks in the UV-Vis optical absorption spectra, obtained by TDDFT calculations using B3LYP functional for all the structures (pristine and doped), is presented in the following tables.

1. Pristine diamond-shaped GQD

Table S3. Information about the excited states contributing to the peaks in the linear optical absorption spectrum of the pristine GQD of D_{2h} symmetry [Fig. 6, main article], computed using the first-principles TDDFT method, and the B3LYP functional.

Peak	Symmetry	E (eV)	f	Wave function
I _y	$^1B_{2u}$	2.31	0.578	$ H \rightarrow L\rangle(0.69200)$
II _x	$^1B_{3u}$	3.46	0.220	$ H - 2 \rightarrow L\rangle(0.53469)$
III _y	$^1B_{2u}$	4.08	0.193	$ H - 1 \rightarrow L + 1\rangle(0.58160)$
IV _y	$^1B_{2u}$	4.90	0.968	$ H - 2 \rightarrow L + 2\rangle(0.44856)$
	$^1B_{2u}$	4.93	0.950	$ H - 2 \rightarrow L + 2\rangle(0.44827)$

2. Doping with single BN-ring

Table S4. Information about the excited states contributing to the peaks in the linear optical absorption spectrum of model 1 of C_{2v} symmetry [Fig. 7(a), main article], computed using the first principles TDDFT method, and the B3LYP functional.

Peak	Symmetry	E (eV)	f	Wave function
I _y	¹ B ₂	2.52	0.427	$ H \rightarrow L\rangle(0.66395)$
II _y	¹ B ₂	3.55	0.748	$ H - 1 \rightarrow L + 1\rangle(0.64281)$
III _x	¹ A ₁	3.83	0.099	$ H - 3 \rightarrow L\rangle(0.53543)$
IV _y	¹ B ₂	4.13	0.017	$ H - 1 \rightarrow L + 2\rangle(0.59847)$
V _x	¹ A ₁	4.56	0.497	$ H - 1 \rightarrow L + 3\rangle(0.44547)$
VI _{xy}	¹ B ₂	4.82	0.059	$ H - 1 \rightarrow L + 4\rangle(0.59345)$
	¹ A ₁	4.84	0.074	$ H - 1 \rightarrow L + 7\rangle(0.63750)$

Table S5. Information about the excited states contributing to the peaks in the linear optical absorption spectrum of model 2 of C_{2v} symmetry [Fig. 7(b), main article], computed using the first-principles TDDFT method, and the B3LYP functional.

Peak	Symmetry	E (eV)	f	Wave function
I _y	¹ B ₂	2.53	0.495	$ H \rightarrow L\rangle(0.68438)$
II _x	¹ A ₁	3.03	0.054	$ H \rightarrow L + 1\rangle(0.63418)$
III _{xy}	¹ B ₂	3.68	0.173	$ H - 1 \rightarrow L + 1\rangle(0.65621)$
	¹ A ₁	3.78	0.092	$ H \rightarrow L + 2\rangle(0.63005)$
IV _y	¹ B ₂	4.10	0.026	$ H - 2 \rightarrow L + 1\rangle(0.34330)$
V _y	¹ B ₂	4.51	0.183	$ H \rightarrow L + 5\rangle(0.47527)$
	¹ B ₂	4.61	0.327	$ H - 1 \rightarrow L + 2\rangle(0.45181)$
VI _y	¹ B ₂	4.99	0.689	$ H - 2 \rightarrow L + 2\rangle(0.56689)$

Table S6. Information about the excited states contributing to the peaks in the linear optical absorption spectrum of model 3 of C_s symmetry [Fig. 7(c), main article], computed using the first-principles TDDFT method, and the B3LYP functional.

Peak	Symmetry	E (eV)	f	Wave function
I _{xy}	¹ A'	1.71	0.441	$ H \rightarrow L\rangle(0.71610)$
II _{xy}	¹ A'	2.37	0.037	$ H - 1 \rightarrow L\rangle(0.53737)$
III _{xy}	¹ A'	3.05	0.209	$ H - 2 \rightarrow L\rangle(0.53447)$
IV _{xy}	¹ A'	3.65	0.064	$ H - 3 \rightarrow L\rangle(0.42588)$
	¹ A'	3.69	0.061	$ H - 1 \rightarrow L + 1\rangle(0.46739)$
V _{xy}	¹ A'	3.89	0.198	$ H - 1 \rightarrow L + 2\rangle(0.46482)$
VI _{xy}	¹ A'	4.08	0.036	$ H - 5 \rightarrow L\rangle(0.46643)$
VII _{xy}	¹ A'	4.60	0.189	$ H - 1 \rightarrow L + 3\rangle(0.39933)$
	¹ A'	4.67	0.283	$ H - 1 \rightarrow L + 3\rangle(0.42775)$

Table S7. Information about the excited states contributing to the peaks in the linear optical absorption spectrum of model 4 of C_s symmetry [Fig. 7(d), main article], computed using the first-principles TDDFT method, and the B3LYP functional.

Peak	Symmetry	E (eV)	f	Wave function
I _{xy}	$^1A'$	2.09	0.581	$ H \rightarrow L\rangle(0.70236)$
II _{xy}	$^1A'$	2.54	0.009	$ H - 1 \rightarrow L\rangle(0.68658)$
III _{xy}	$^1A'$	2.84	0.026	$ H \rightarrow L + 1\rangle(0.66242)$
IV _{xy}	$^1A'$	3.30	0.026	$ H \rightarrow L + 3\rangle(0.50235)$
V _{xy}	$^1A'$	3.56	0.143	$ H - 2 \rightarrow L\rangle(0.44978)$
VI _{xy}	$^1A'$	4.07	0.085	$ H - 4 \rightarrow L\rangle(0.56338)$
VII _{xy}	$^1A'$	4.28	0.220	$ H - 1 \rightarrow L + 2\rangle(0.47600)$
VIII _{xy}	$^1A'$	4.85	0.226	$ H - 3 \rightarrow L + 1\rangle(0.50758)$

3. Doping with two fused BN-rings

Table S8. Information about the excited states contributing to the peaks in the linear optical absorption spectrum of model 5 of C_s symmetry [Fig. 8(a), main article], computed using the first-principles TDDFT method, and the B3LYP functional.

Peak	Symmetry	E (eV)	f	Wave function
I _{xy}	$^1A'$	1.77	0.436	$ H \rightarrow L\rangle(0.69855)$
II _{xy}	$^1A'$	2.38	0.114	$ H \rightarrow L + 1\rangle(0.50494)$
III _{xy}	$^1A'$	2.66	0.128	$ H - 1 \rightarrow L\rangle(0.48027)$
IV _{xy}	$^1A'$	2.89	0.009	$ H \rightarrow L + 2\rangle(0.66386)$
V _{xy}	$^1A'$	3.39	0.216	$ H - 2 \rightarrow L\rangle(0.57870)$
VI _{xy}	$^1A'$	3.82	0.122	$ H - 3 \rightarrow L\rangle(0.41818)$
VII _{xy}	$^1A'$	4.27	0.045	$ H - 5 \rightarrow L\rangle(0.34716)$
VIII _{xy}	$^1A'$	4.71	0.160	$ H - 6 \rightarrow L\rangle(0.44332)$
	$^1A'$	4.76	0.157	$ H - 1 \rightarrow L + 4\rangle(0.43532)$

Table S9. Information about the excited states contributing to the peaks in the linear optical absorption spectrum of model 6 of C_s symmetry [Fig. 8(b), main article], computed using the first-principles TDDFT method, and the B3LYP functional.

Peak	Symmetry	E (eV)	f	Wave function
I _{xy}	$^1A'$	2.44	0.416	$ H \rightarrow L\rangle(0.66788)$
II _{xy}	$^1A'$	3.03	0.039	$ H \rightarrow L + 1\rangle(0.68229)$
III _{xy}	$^1A'$	3.50	0.024	$ H \rightarrow L + 2\rangle(0.47925)$
IV _{xy}	$^1A'$	3.78	0.571	$ H - 1 \rightarrow L + 1\rangle(0.56118)$
V _{xy}	$^1A'$	4.07	0.230	$ H - 1 \rightarrow L + 2\rangle(0.58977)$
VI _{xy}	$^1A'$	4.67	0.134	$ H - 1 \rightarrow L + 5\rangle(0.58280)$

Table S10. Information about the excited states contributing to the peaks in the linear optical absorption spectrum of model 7 of C_{2v} symmetry [Fig. 8(c), main article], computed using the first-principles TDDFT method, and the B3LYP functional.

Peak	Symmetry	E (eV)	f	Wave function
I _y	¹ B ₂	1.17	0.260	$ H \rightarrow L\rangle(0.75936)$
II _x	¹ A ₁	1.99	0.014	$ H - 1 \rightarrow L\rangle(0.69825)$
III _{xy}	¹ A ₁	2.50	0.018	$ H \rightarrow L + 1\rangle(0.68531)$
	¹ B ₂	2.54	0.072	$ H - 2 \rightarrow L\rangle(0.65599)$
IV _y	¹ B ₂	2.85	0.124	$ H \rightarrow L + 2\rangle(0.64371)$
V _x	¹ A ₁	3.18	0.103	$ H \rightarrow L + 5\rangle(0.60398)$
VI _x	¹ A ₁	3.66	0.019	$ H \rightarrow L + 9\rangle(0.66119)$
VII _y	¹ B ₂	4.32	0.308	$ H - 1 \rightarrow L + 3\rangle(0.53077)$
VIII _x	¹ A ₁	4.55	0.138	$ H - 2 \rightarrow L + 1\rangle(0.51314)$

Table S11. Information about the excited states contributing to the peaks in the linear optical absorption spectrum of model 8 of C_s symmetry [Fig. 8(d), main article], computed using the first-principles TDDFT method, and the B3LYP functional.

Peak	Symmetry	E (eV)	f	Wave function
I _{xy}	¹ A'	1.23	0.170	$ H \rightarrow L\rangle(0.71559)$
II _{xy}	¹ A'	1.79	0.093	$ H - 1 \rightarrow L\rangle(0.62914)$
III _{xy}	¹ A'	2.93	0.513	$ H - 1 \rightarrow L + 1\rangle(0.66382)$
IV _{xy}	¹ A'	3.36	0.032	$ H \rightarrow L + 5\rangle(0.68594)$
V _{xy}	¹ A'	3.56	0.032	$ H - 3 \rightarrow L\rangle(0.47538)$
	¹ A'	3.62	0.033	$ H \rightarrow L + 8\rangle(0.50498)$
VI _{xy}	¹ A'	3.79	0.119	$ H \rightarrow L + 9\rangle(0.44030)$
	¹ A'	3.81	0.054	$ H - 1 \rightarrow L + 2\rangle(0.55266)$
VII _{xy}	¹ A'	4.11	0.056	$ H - 1 \rightarrow L + 2\rangle(0.55266)$
VIII _{xy}	¹ A'	4.35	0.149	$ H \rightarrow L + 4\rangle(0.59709)$

4. Doping with two separated BN-rings

Table S12. Information about the excited states contributing to the peaks in the linear optical absorption spectrum of model 9 ($\uparrow - \uparrow$) of C_{2v} symmetry [Fig. 9(a), main article], computed using the first-principles TDDFT method, and the B3LYP functional.

Peak	Symmetry	E (eV)	f	Wave function
I _y	¹ B ₂	2.75	0.393	$ H \rightarrow L\rangle(0.67093)$
II _x	¹ A ₁	3.62	0.168	$ H - 2 \rightarrow L\rangle(0.53655)$
III _y	¹ B ₂	3.98	0.247	$ H - 1 \rightarrow L + 2\rangle(0.45296)$
	¹ B ₂	4.03	0.265	$ H - 1 \rightarrow L + 1\rangle(0.44186)$
IV _x	¹ A ₁	4.51	0.009	$ H - 1 \rightarrow L + 3\rangle(0.65830)$
V _y	¹ B ₂	4.80	0.486	$ H - 2 \rightarrow L + 2\rangle(0.65482)$

Table S13. Information about the excited states contributing to the peaks in the linear optical absorption spectrum of model 9 ($\uparrow - \downarrow$) of D_{2h} symmetry [Fig. 9(d), main article], computed using the first-principles TDDFT method, and the B3LYP functional.

Peak	Symmetry	E (eV)	f	Wave function
I _y	¹ B _{2u}	2.79	0.399	$ H \rightarrow L\rangle(0.67381)$
II _y	¹ B _{2u}	4.06	0.650	$ H - 2 \rightarrow L + 1\rangle(0.62120)$
III _y	¹ B _{2u}	4.32	0.069	$ H \rightarrow L + 3\rangle(0.64725)$
IV _x	¹ B _{3u}	4.72	0.010	$ H - 7 \rightarrow L\rangle(0.65575)$
V _x	¹ B _{3u}	4.95	0.067	$ H \rightarrow L + 5\rangle(0.57600)$
VI _x	¹ B _{3u}	5.18	0.056	$ H - 4 \rightarrow L + 1\rangle(0.64487)$

Table S14. Information about the excited states contributing to the peaks in the linear optical absorption spectrum of model 10 ($\uparrow - \uparrow$) of C_{2v} symmetry [Fig. 9(b), main article], computed using the first-principles TDDFT method, and the B3LYP functional.

Peak	Symmetry	E (eV)	f	Wave function
I _y	¹ B ₂	1.27	0.348	$ H \rightarrow L\rangle(0.76497)$
II _x	¹ A ₁	1.66	0.010	$ H \rightarrow L + 1\rangle(0.50669)$
III _x	¹ A ₁	2.38	0.006	$ H \rightarrow L + 2\rangle(0.55592)$
IV _x	¹ A ₁	2.86	0.260	$ H - 2 \rightarrow L\rangle(0.54839)$
V _y	¹ B ₂	3.69	0.145	$ H - 1 \rightarrow L + 2\rangle(0.45314)$
VI _x	¹ A ₁	4.27	0.019	$ H \rightarrow L + 4\rangle(0.52350)$
VII _x	¹ A ₁	4.52	0.052	$ H - 1 \rightarrow L + 4\rangle(0.68022)$

Table S15. Information about the excited states contributing to the peaks in the linear optical absorption spectrum of model 10 ($\uparrow - \downarrow$) of C_{2h} symmetry [Fig. 9(e), main article], computed using the first-principles TDDFT method, and the B3LYP functional.

Peak	Symmetry	E (eV)	f	Wave function
I _{xy}	¹ B _u	1.46	0.433	$ H \rightarrow L\rangle(0.74266)$
II _{xy}	¹ B _u	2.28	0.041	$ H \rightarrow L + 2\rangle(0.54892)$
III _{xy}	¹ B _u	2.71	0.192	$ H - 2 \rightarrow L\rangle(0.53178)$
IV _{xy}	¹ B _u	3.49	0.287	$ H - 1 \rightarrow L + 1\rangle(0.67251)$
V _{xy}	¹ B _u	3.73	0.101	$ H - 3 \rightarrow L\rangle(0.66967)$
VI _{xy}	¹ B _u	4.22	0.081	$ H - 2 \rightarrow L + 2\rangle(0.53063)$
VII _{xy}	¹ B _u	4.49	0.095	$ H - 6 \rightarrow L\rangle(0.53501)$

Table S16. Information about the excited states contributing to the peaks in the linear optical absorption spectrum of model 11 ($\uparrow - \uparrow$) of C_s symmetry [Fig. 9(c), main article], computed using the first-principles TDDFT method, and the B3LYP functional.

Peak	Symmetry	E (eV)	f	Wave function
I _{xy}	¹ A'	1.59	0.354	$ H \rightarrow L\rangle(0.71146)$
II _{xy}	¹ A'	2.68	0.102	$ H - 1 \rightarrow L\rangle(0.57517)$
III _{xy}	¹ A'	3.01	0.029	$ H - 2 \rightarrow L\rangle(0.46478)$
IV _{xy}	¹ A'	3.33	0.412	$ H - 3 \rightarrow L\rangle(0.41918)$
V _{xy}	¹ A'	3.63	0.053	$ H \rightarrow L + 5\rangle(0.52268)$
VI _{xy}	¹ A'	3.88	0.065	$ H - 4 \rightarrow L\rangle(0.65638)$
VII _{xy}	¹ A'	4.29	0.442	$ H - 1 \rightarrow L + 1\rangle(0.59132)$
VIII _{xy}	¹ A'	4.75	0.046	$ H - 2 \rightarrow L + 2\rangle(0.63143)$

Table S17. Information about the excited states contributing to the peaks in the linear optical absorption spectrum of model 11 ($\uparrow - \downarrow$) of C_{2h} symmetry [Fig. 9(f), main article], computed using the first-principles TDDFT method, and the B3LYP functional.

Peak	Symmetry	E (eV)	f	Wave function
I _{xy}	1B_u	1.73	0.556	$ H \rightarrow L\rangle(0.73133)$
II _{xy}	1B_u	2.63	0.021	$ H - 2 \rightarrow L\rangle(0.59122)$
III _{xy}	1B_u	2.92	0.053	$ H \rightarrow L + 2\rangle(0.58383)$
IV _{xy}	1B_u	3.42	0.303	$ H \rightarrow L + 3\rangle(0.56829)$
V _{xy}	1B_u	4.11	0.434	$ H - 1 \rightarrow L + 1\rangle(0.51329)$
VI _{xy}	1B_u	4.61	0.353	$ H - 3 \rightarrow L + 1\rangle(0.59960)$

C. Orbital Projected Density of States

In Fig. S1 we present the plots of both total and the orbital-projected density of states (DOS) for the pristine GQD as well as a few BN-GQDs. We note that for all the structures, the p -orbitals, but more specifically π/π^* orbitals, dominate the total DOS near the Fermi level, consistent with their planar geometries.

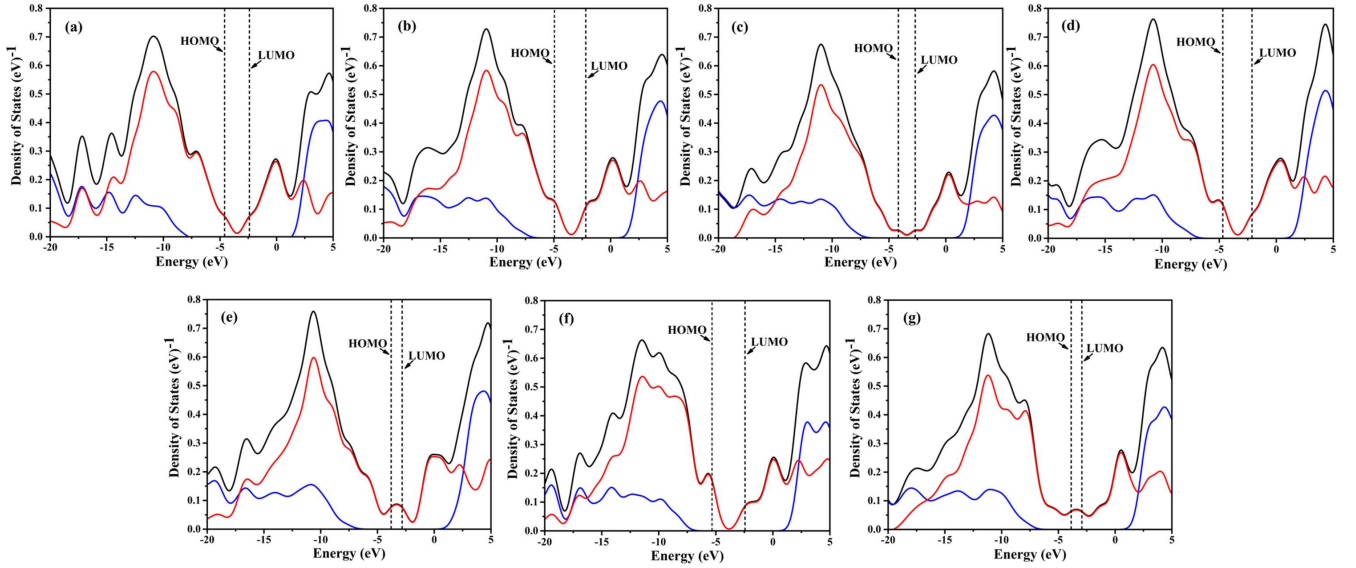


Figure S1. Total and orbital projected density of states (DOS) plots for: pristine GQD [(a)], single BN-ring doping [(b) model 1, (c) model 3], fused double BN-ring doping [(d) model 6, (e) model 7], separated double BN-ring doping [(f) Model 9 ($\uparrow - \downarrow$), (g) model 10 ($\uparrow - \uparrow$)]. Here black lines denote the total density of states (TDOS), while red and blue lines represent the partial DOS corresponding to the contributions of the p and s orbitals, respectively.

D. Comparison between absorption spectra computed using different functionals

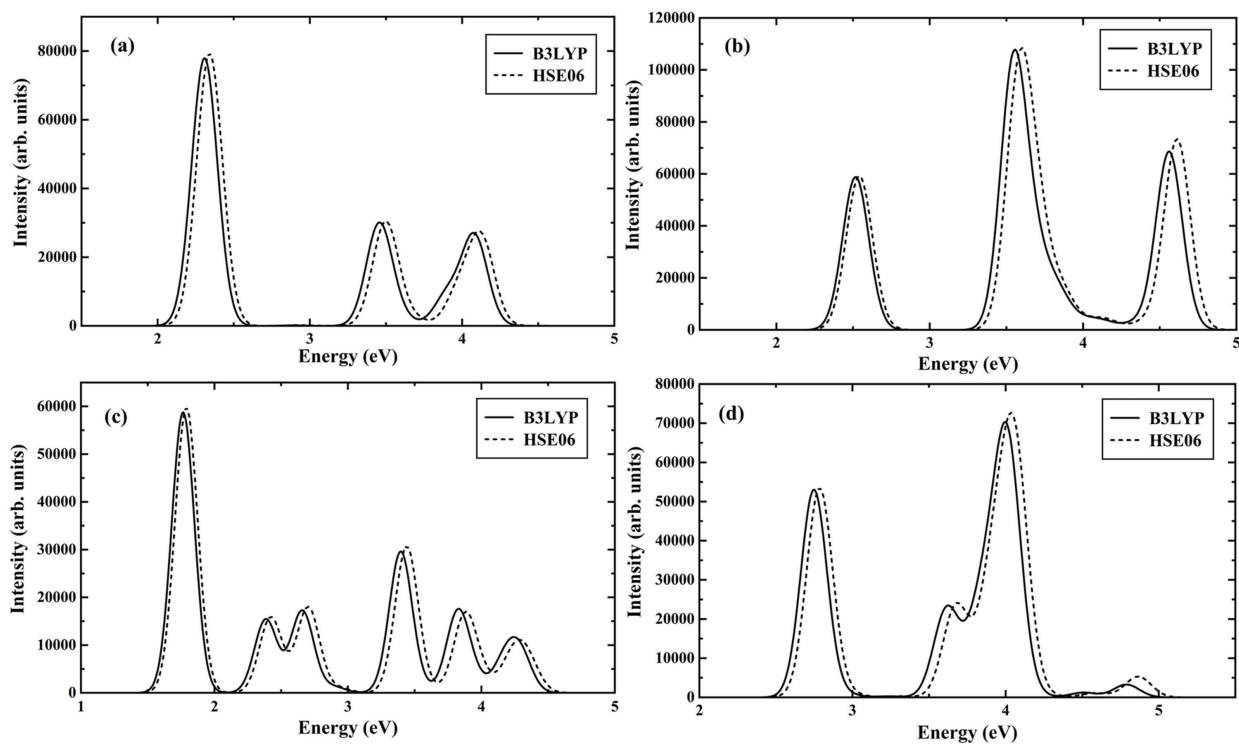


Figure S2. Comparison of TDDFT UV-Vis absorption spectra obtained with B3LYP and HSE06 functionals with 20 excited states: (a) pristine GQD, (b) single BN-ring doping (model 1), (c) fused double BN-ring doping (model 5), (d) separated double BN-ring doping (model 9 ($\uparrow - \uparrow$)).

E. Absorption spectra calculated with different numbers of excited states

UV-Vis absorption spectra were calculated with different numbers of excited states to check convergence using the TDDFT-B3LYP level of theory.

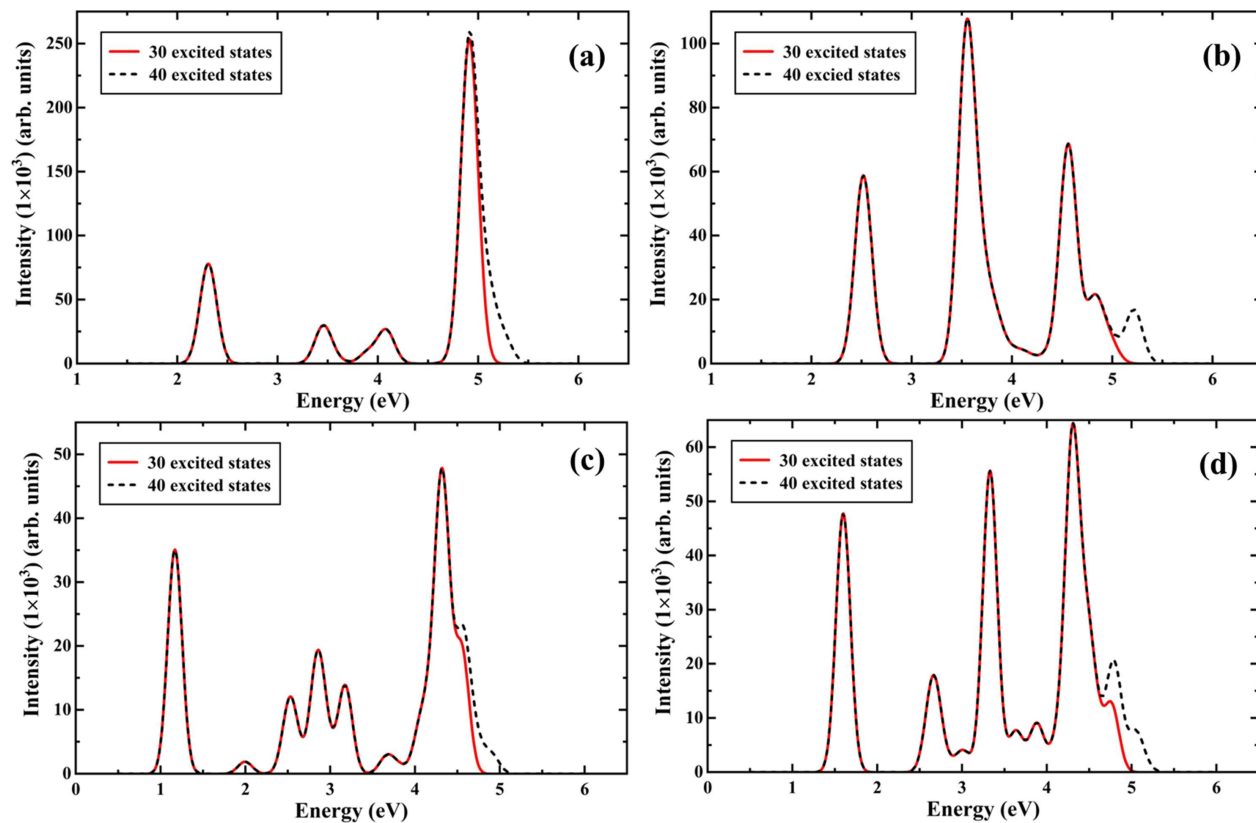


Figure S3. (a) pristine GQD; (b) single BN-ring doping (model 1); (c) fused double BN-ring doping (model 7); (d) separated double BN-ring doping (model 11 ($\uparrow - \uparrow$)).

F. Comparison of UV-Vis absorption spectra (TDDFT-B3LYP) for doped and pristine GQDs

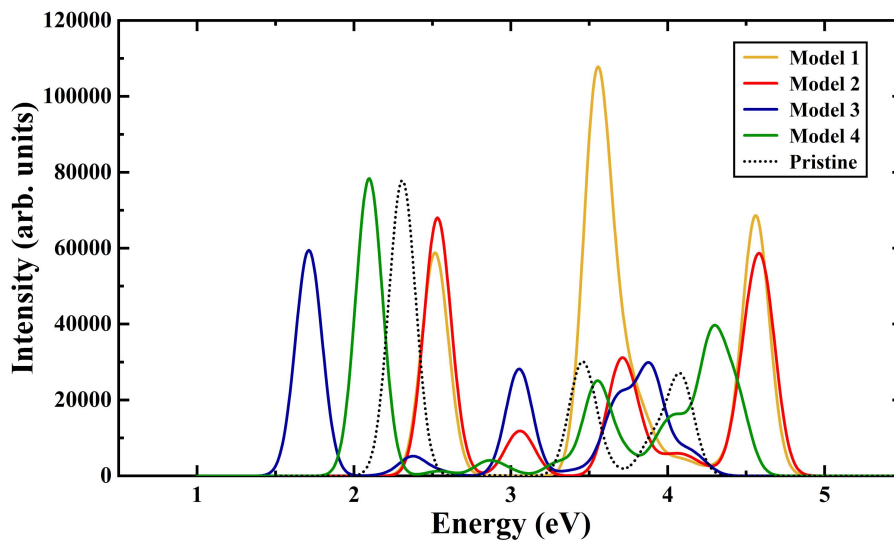


Figure S4. UV-Vis absorption spectra of single BN-ring doped BN-GQDs compared to that of the pristine GQD, computed at the TDDFT-B3LYP level of theory.

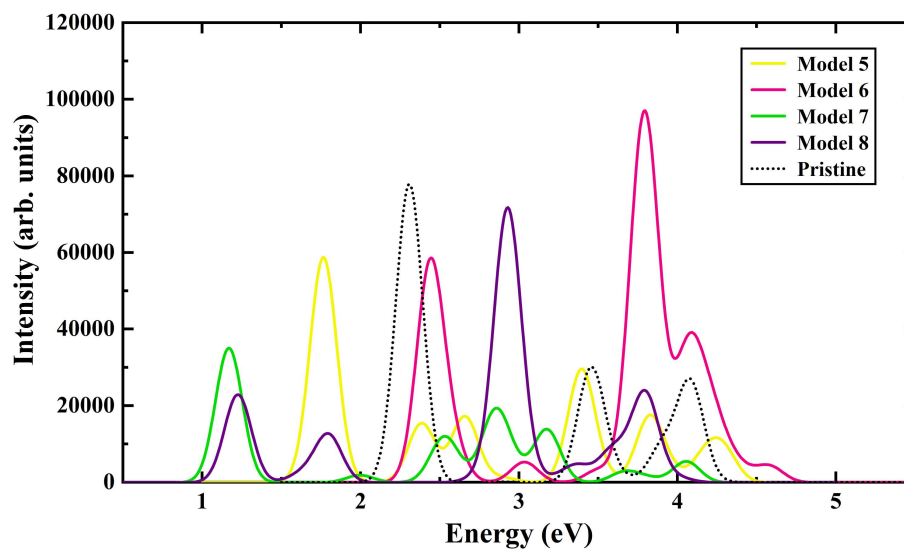


Figure S5. UV-Vis absorption spectra of BN-GQDs doped by two fused BN-rings, compared to that of the pristine GQD, computed at the TDDFT-B3LYP level of theory.

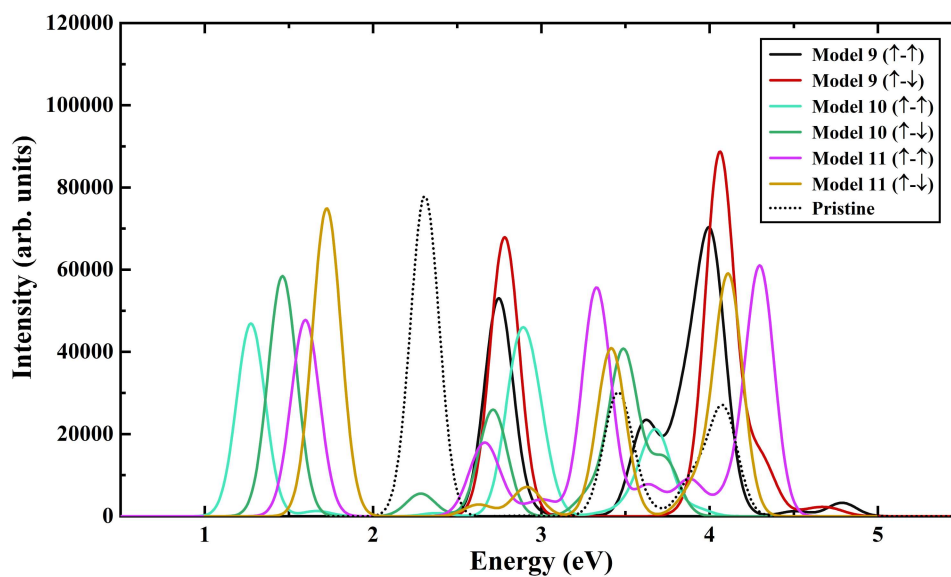


Figure S6. UV-Vis absorption spectra of BN-GQDs doped by two separated BN-rings, compared to that of the pristine GQD, computed at the TDDFT-B3LYP level of theory.